Effect of Porosity and Permeability Evolution on Injection-Induced Aseismic Slip

Yuyun Yang[1], **Eric M. Dunham**[1,2]

[1]Institute for Computational and Mathematical Engineering, Stanford University
[2]Department of Geophysics, Stanford University

Key Points:

- Modeling of constant rate fluid injection into a fault predicts steadily propagating aseismic slip front
- Migration rate of aseismic slip front increases with injection rate and ranges from less than 50 to 1000 m/day for typical parameters
- Dilatancy and permeability enhancement alter system response as compared to linear pore pressure diffusion

Corresponding author: Yuyun Yang, yyang85@stanford.edu

Abstract

It is widely recognized that fluid injection can trigger fault slip. However, the processes by which the fluid-rock interactions facilitate or inhibit slip are poorly understood and some are neglected or oversimplified in most models of injection-induced slip. In this study, we perform a 2D antiplane shear investigation of aseismic slip that occurs in response to fluid injection into a permeable fault governed by rate-and-state friction. We account for pore dilatancy and permeability changes that accompany slip, and quantify how these processes affect pore pressure diffusion, which couples to aseismic slip. The fault response to injection has two phases. In the first phase, slip is negligible and pore pressure closely follows the standard linear diffusion model. Pressurization of the fault eventually triggers aseismic slip in the immediate vicinity of the injection site. In the second phase, the aseismic slip front expands outward and dilatancy causes pore pressure to depart from the linear diffusion model. Aseismic slip front overtakes pore pressure contours, with both subsequently advancing at constant rate along fault. We quantify how prestress, initial state variable, injection rate, and frictional properties affect the migration rate of the aseismic slip front, finding values ranging from less than 50 to 1000 m/day for typical parameters. Additionally, we compare to the case when porosity and permeability evolution are neglected. In this case, the aseismic slip front migration rate and total slip are much higher. Our modeling demonstrates that porosity and permeability evolution, especially dilatancy, fundamentally alters how faults respond to fluid injection.

Plain Language Summary

The underground injection of fluids during wastewater disposal, geothermal operations, and other energy-production activities has been linked to the occurrence of earthquakes. In addition to earthquakes, fluid injection can also trigger aseismic slip on faults, that is, frictional sliding that occurs so slowly that seismic waves and ground shaking are not produced. Here we perform computer modeling of fluid injection and aseismic slip, exploring how the injection rate and fluid transport properties influence the aseismic slip response. We speculate that additional complexity in frictional properties and other conditions would cause aseismic slip to be accompanied by numerous, small earthquakes (microseismicity), as is often observed during injection. We quantify the rate at which aseismic slip migrates outward from the injection site and compare predicted migration rates to observed microseismicity patterns. Our model also predicts fluid pressure changes, slip, rock deformation surrounding the fault, and fluid flow paths that might be measurable and used to validate the modeling.

1 Introduction

Fluid injection has been associated with the triggering of seismic events in geologically stable regions that previously had minimal detected seismicity (McGarr et al., 2015). Injection is done in the context of wastewater disposal and hydraulic fracturing in oil and gas operations, carbon sequestration, and geothermal energy production (Mazzoldi et al., 2012; Ellsworth, 2013; Elsworth et al., 2016). Many sequences of small earthquakes have been recorded near injection wells, some of which last for months or years (Horton, 2012; W. Y. Kim, 2013; Wei et al., 2015; Goebel et al., 2016; Eyre et al., 2020). Injection not only triggers microseismic events, but is also capable of triggering damaging earthquakes such as the 2011 M_w 5.7 and 2016 M_w 5.8 events in Oklahoma (Keranen et al., 2013; Yeck et al., 2017), as well as the 2017 M_w 5.4 event in Pohang, South Korea (K. H. Kim et al., 2018). This problem not only impacts the lives of people who face the risk of damaging earthquakes in the affected areas, but also bears important implications for harnessing the Earth's natural resources safely and responsibly. To effectively assess earthquake hazards, a better understanding of the physical mechanisms underlying fluid-induced seismicity is essential.

Several processes have been proposed as the triggering mechanism of injection-induced seismicity. One of them is pore pressure diffusion (Shapiro et al., 1997; Shapiro & Dinske, 2009), where pressure perturbations expanding out from the injection site reduce the effective normal stress of the rock matrix, bringing the rock closer to the Coulomb-Mohr failure criterion (Handin, 1969). Later work has also investigated poroelastic stress changes, which may dominate over pore pressure at large distances (Segall & Lu, 2015; Chang & Segall, 2016; Goebel et al., 2017; Goebel & Brodsky, 2018; Szafranski & Duan, 2020), as the solid matrix at some distance from the injection point initially responds elastically to fluid injection, promoting critically stressed faults to failure before the arrival of diffusive pressure perturbations (Deng et al., 2016). Recently, fault loading and reactivation by aseismic slip has been proposed as another mechanism that is able to transmit elastic stresses far beyond the pressure contours (Guglielmi et al., 2015; Wei et al., 2015; Bhattacharya & Viesca, 2019; Eyre et al., 2019). Aseismic slip is also thought to play an important role in the propagation of earthquake swarms, which could be composed of bursts of seismicity with migration velocity consistent with slow slip migration (Roland & McGuire, 2009; Wei et al., 2015; Shelly et al., 2016; De Barros et al., 2020). Aseismic slip triggered by fluid injection is the focus of our study.

The injection of fluid into a fault not only alters pore pressure and triggers slip, but also changes properties of the fault zone that in turn impact fluid flow and fault slip behavior. The most relevant properties here are porosity and permeability. Many experiments, in both the laboratory and in situ, show that dilatancy (the expansion of pores and the fluids within them) accompanies shear deformation of fault zone rocks (Morrow & Byerlee, 1989; Rawling et al., 2002; Samuelson et al., 2009; Guglielmi et al., 2015; Cappa et al., 2018; Proctor et al., 2020; Brantut, 2020). In the absence of fluid flow (i.e., undrained conditions), dilatancy reduces pore pressure, thus increasing the effective normal stress and stabilizing the fault (Lockner & Byerlee, 1994; Segall & Rice, 1995; Segall et al., 2010). Porosity changes also alter permeability. As the pores dilate and more porous space becomes connected, permeability is enhanced (Zhu & Wong, 1999; Simpson et al., 2001; Y. Zhang et al., 2008; Ye & Ghassemi, 2018). This facilitates fluid flow and enables pore pressure perturbations to reach greater distances along the fault in a shorter period of time. Pore dilation and permeability enhancement on rough slip surface also depends on the nature of the surface contacts. Initially mated surfaces exhibit more significant dilation and permeability enhancement with slip, whereas on unmated surfaces, compaction and permeability reduction may result from the comminution of surface asperities (Im et al., 2019). Likewise, experiments involving shearing of fluid-saturated gouge have also shown both stabilization from dilatancy and destabilization from compaction. It is certainly evident that the evolution of porosity and permeability, while complex, can fundamentally influence fluid flow and fault slip behavior, and therefore needs to be taken into account in fault models with hydromechanical coupling.

Recently, there have been several modeling efforts to characterize the aseismic slip resulting from fluid injection and how that could potentially affect resulting earthquakes. Garagash and Germanovich (2012) studied injection into a slip-weakening fault, highlighting the key role that prestress (relative to static and dynamic frictional strength) plays in controlling whether slip is seismic or aseismic. Bhattacharya and Viesca (2019) modeled quasi-static slip with linear slip-weakening friction, adding step changes in permeability in order to fit injection experiment results from Guglielmi et al. (2015). Eyre et al. (2019) conducted modeling in the context of hydraulic fracturing with rate-and-state friction and flash heating to show that aseismic slip could progressively load distal, unstable regions of a fault. Dublanchet (2019) quantified the propagation of aseismic slip on a velocity-strengthening rate-and-state fault, showing how different prestresses, frictional conditions, hydraulic properties and injection history control the dynamics of fluid-induced aseismic slip. Wynants-Morel et al. (2020) used 3D hydromechanical modeling on a permeable, slip-weakening fault to characterize slip resulting from different prestress conditions, and was able to generate features observed in induced earthquake

sequences. Larochelle et al. (2020) studied how fault prestress, relative to static or dynamic frictional strength, controls whether slip is confined to the fluid-affected zone or expands beyond it. Other studies have accounted for the full poroelastic response in addition to rate-and-state friction (Pampillón et al., 2018; Torberntsson et al., 2018; Heimisson et al., 2019; Andrés et al., 2019). These, and other, numerical modeling efforts were able to explain a wide range of observations in the lab and field, as well as to provide insight into various hydromechanical processes. We build on these important studies by adopting a more comprehensive modeling approach, incorporating rate-and-state friction as well as the evolution of porosity and permeability that accompanies slip and pore pressure diffusion, which could have significant effects on the nature of the fault slip.

In this study, we investigate the propagation of aseismic slip that is triggered by fluid injection. This is done in 2D antiplane shear for a planar, permeable fault in a homogeneous elastic solid. The fault is governed by rate-and-state friction with the slip law of state evolution. Fluids are confined to the fault, and injection occurs at a specified rate into the center of the fault. Porosity and permeability evolve with slip, with permeability related to porosity via a power-law relation. The goal of this study is to evaluate the controlling factors for the initiation and propagation of aseismic slip, and to make testable predictions of potentially observable quantities like the migration rate of the aseismic slip and pore pressure contours, as a function of prestress, frictional parameters, and injection rate. Section 2 introduces the governing equations we use for the fault, fluid transport, and porosity and permeability evolution. Section 3 lists model parameters and displays the simulation results. We showcase comparisons for different prestress conditions, initial state variables, injection rates, and frictional properties, evaluating their relative importance in determining slip behavior. We also highlight how neglecting porosity and permeability evolution can drastically change the nature of fault slip. Finally, in Section 4, we connect our simulations with a limited set of observations and emphasize the important role of hydromechanical coupling in characterizing fault response to fluid injection.

2 Governing Equations

2.1 Fault Model

We consider the 2D antiplane shear problem of a planar fault embedded in a linear elastic medium (Figure 1). The fault has constant total normal stress σ_n and constant initial shear stress τ_0. The fault is located at $y = 0$, and displacements $u(y, z, t)$ (about the prestressed initial state) are in the x-direction. For computational efficiency, we assume symmetry about the fault, enabling us to model only half the domain ($y \geq 0$). The governing equations for quasi-static antiplane shear deformation of an elastic solid are

$$\frac{\partial \sigma_{xy}}{\partial x} + \frac{\partial \sigma_{xz}}{\partial z} = 0, \quad \sigma_{xy} = \mu \frac{\partial u}{\partial y}, \quad \sigma_{xz} = \mu \frac{\partial u}{\partial z}, \tag{1}$$

where σ_{xy} and σ_{xz} are the quasi-static stress changes associated with displacement u and μ is the shear modulus, which we assume is constant. We define slip and slip velocity as

$$\delta(z, t) = 2u(0, z, t) \quad \text{and} \quad V = \frac{\partial \delta}{\partial t}, \tag{2}$$

respectively. The fault boundary conditions are

$$\tau = f(\Psi, V)\bar{\sigma}_n, \tag{3}$$

$$\dot{\Psi} = G(\Psi, V), \tag{4}$$

where τ is the shear stress and Ψ is the state variable. Equation (3) sets the shear stress equal to the frictional strength, with $f(\Psi, V)$ being the rate-and-state friction coefficient and $\bar{\sigma}_n = \sigma_n - p$ the effective normal stress calculated as the difference between the total normal stress σ_n and pore pressure p. Equation (4) is the state evolution equation.

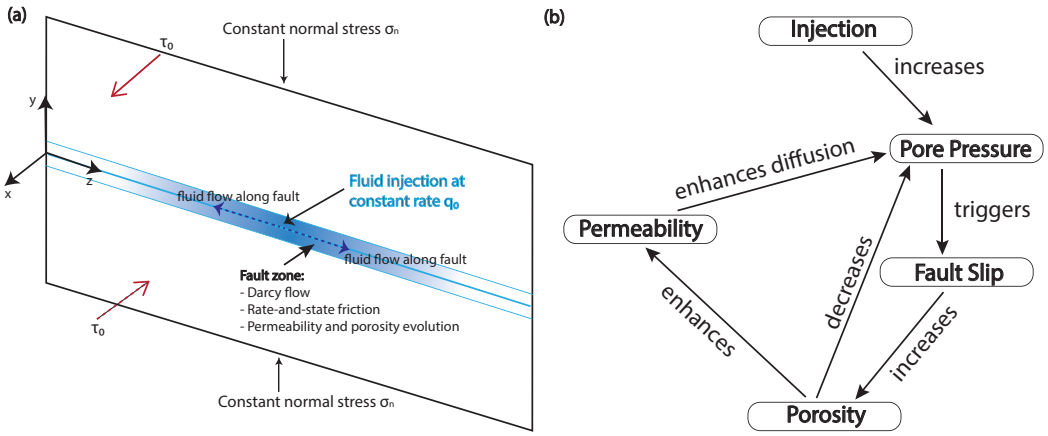

Figure 1. (a) The 2D antiplane problem with fluid injection in the middle of the fault and along-fault flow through a permeable fault zone. (b) Feedback relations among pore pressure, fault slip, porosity and permeability.

For the shear stress computation, we switch between the quasi-dynamic approximation with radiation damping (Rice, 1993) at low slip velocities (for which the radiation-damping term is effectively negligible) and a dynamic solver with full inertial effects at high slip velocities (Duru et al., 2019). In the quasi-dynamic approximation,

$$\tau(z,t) = \tau_0 + \sigma_{xy}(0,z,t) - \eta_{rad}V, \tag{5}$$

where τ_0 is the initial shear stress and η_{rad} is the radiation damping parameter (Rice, 1993). In the dynamic solver, we add the inertial term $\rho\partial^2 u/\partial t^2$, involving density ρ, to the momentum balance (1) and disable radiation damping. Switching between quasi-dynamic and fully dynamic solvers is based on the nondimensional ratio $R = \eta_{rad}V/\tau_{qs}$, where the numerator is the radiation damping term and the denominator is the quasi-static shear stress (Duru et al., 2019). We choose $R = 10^{-3}$ to control switching into and out of the fully dynamic solver. For the computation of the rate-and-state friction coefficient, we use the regularized form (Rice et al., 2001):

$$f(\Psi,V) = a\sinh^{-1}\left(\frac{V}{2V_0}\exp\{\Psi/a\}\right) \approx a\ln\left(\frac{V}{V_0}\right) + \Psi, \tag{6}$$

where a is the direct effect parameter and V_0 is the reference velocity. The approximate form is valid for $\tau/(a\bar{\sigma}) \ll 1$, a condition that is met in all of our simulations. Our choice of state variable, Ψ, is dimensionless and of order unity, making it ideally suited for numerical calculations. The change of variable $\Psi = f_0 + b\ln(V_0\theta/d_c)$, for state evolution distance d_c, state evolution parameter b, and state variable θ having units of time, brings this into the more common form, $f \approx f_0 + a\ln(V/V_0) + b\ln(V_0\theta/d_c)$.

We use the slip law (Ruina, 1983) for state evolution, as there is evidence it matches the stress data from large velocity step increases, decreases, and load point holds better than the aging law (Bhattacharya et al., 2017). We have written the slip law in the following form:

$$G(\Psi,V) = -\frac{V}{d_c}[f(\Psi,V) - f_{ss}(V)], \tag{7}$$

where

$$f_{ss}(V) = f_0 + (a-b)\log\left(\frac{V}{V_0}\right) \tag{8}$$

is the steady state friction coefficient. This coincides with the usual form of the slip law when written in terms of θ.

Apart from the fault boundary condition, the computational domain has three other boundary conditions:

$$\sigma_{xz}(y,0,t)=0, \quad \sigma_{xz}(y,L_z,t)=0, \quad u(L_y,z,t)=0, \tag{9}$$

where L_y and L_z are dimensions of the domain in the y and z directions. The boundaries perpendicular to the fault are traction-free, and zero-displacement condition on the remote boundary parallel to the fault indicates that there is no remote plate loading incorporated in this model. We use a 50 km $\times$ 50 km domain such that the simulation results are relatively insensitive to the remote boundaries. Since we are considering a very short time interval on the scale of days, effects from plate loading can be ignored.

2.2 Fluid Model

Our idealized fluid transport model, like many others in the literature (Walder & Nur, 1984; Rice, 1992; Wiprut & Zoback, 2000; Saffer & Tobin, 2011; McClure & Horne, 2011; Yamashita, 2013; Bhattacharya & Viesca, 2019; Zhu et al., 2020; Larochelle et al., 2020), accounts only for along-fault flow. This is motivated by the commonly observed fault zone structure of a permeable damage zone embedded within relatively impermeable host rock (Faulkner & Rutter, 2001; Wibberley, 2002). Fault-normal flow is also limited by the anisotropic permeability structure of the damage zone, which generally features much higher permeability in the fault-parallel direction than in the fault-normal direction (Faulkner & Rutter, 2001). Nonetheless, the stabilizing effects of dilatancy are likely to be mitigated, to some extent, by fault-normal flow (Segall & Rice, 1995; Segall et al., 2010), and arguably the most important extension to our current study would be to account for this fault-normal flow. Our fluid transport model applies equally well to the case of smaller faults or fracture systems without well-developed damage zones, in which fluid flow is restricted to the rough fault interface. The idealization of fracture flow has been widely used in the porous flow community for studying fractured reservoirs in otherwise low permeability formations, and has been applied in simulations that couple with rate-and-state frictional sliding (McClure & Horne, 2011; Norbeck & Horne, 2018).

The continuity of fluid mass, in the absence of fluid sources or sinks, can be expressed as

$$\frac{\partial m}{\partial t}+\frac{\partial(\rho q)}{\partial z}=0, \tag{10}$$

where m is the fluid mass per unit volume of rock, ρ is the fluid density, and q is the fluid volume flux per unit area of the porous solid (i.e., Darcy velocity). Since $m=\rho\phi$, where ϕ is the rock porosity or pore volume fraction, we can write

$$\dot{m}=\rho\dot{\phi}+\phi\dot{\rho}=\rho\dot{\phi}+\phi(\rho\beta_f\dot{p}), \tag{11}$$

where $\beta_f=\rho^{-1}\partial\rho/\partial p$ is the fluid compressibility, and the overdot represents the partial time derivative (H. F. Wang, 2017).

Inelastic strains during fluid transport and deformation can induce inelastic porosity changes, which influence fluid transport properties (Wong et al., 1997). If the change in porosity is written as the sum of an elastic and a plastic component, $\dot{\phi}=\phi\beta_\phi\dot{p}+\dot{\phi}_p$ (Walder & Nur, 1984; Segall & Rice, 1995), then

$$\dot{m}=\phi\rho\beta_f\dot{p}+\rho(\phi\beta_\phi\dot{p}+\dot{\phi}_p)=\rho(\phi\beta\dot{p}+\dot{\phi}_p), \tag{12}$$

where $\beta_\phi=\phi^{-1}\partial\phi/\partial p$ is the elastic pore compressibility at fixed normal stress and fixed fault-parallel strains (Walder & Nur, 1984; Segall & Rice, 1995; Rice, 2006). The combined fluid and elastic pore compressibility is $\beta=\beta_f+\beta_\phi$. We have chosen $\beta_\phi=0.45$

188 GPa^{-1}, which is within the range of foliated gouge compressibility data compiled by Wibberley
189 (2002), and $\beta_f = 0.55\ \mathrm{GPa}^{-1}$, which is within the range of water compressibility dis-
190 cussed in Mase and Smith (1987). Therefore $\beta = 1\ \mathrm{GPa}^{-1}$.

Fluid volume flux q is given by Darcy's law:

$$q = -\frac{k}{\eta}\frac{\partial p}{\partial z}, \tag{13}$$

where k is the permeability, η is the fluid viscosity, and the effects of gravity are neglected (e.g., as appropriate for flow in the horizontal direction). We rewrite the fluid mass conservation by substituting Equations (12) and (13) into Equation (10) and add a source term for fluid injection:

$$\phi\beta\frac{\partial p}{\partial t} = \frac{\partial}{\partial z}\left(\frac{k}{\eta}\frac{\partial p}{\partial z}\right) - \frac{\partial \phi_p}{\partial t} + q_0\delta(z), \tag{14}$$

191 where q_0 is a constant injection rate (volume per time per unit distance in the x direc-
192 tion) that is turned on at the start of our simulations ($t = 0$), and $\delta(z)$ is the Dirac delta
193 function that places the source at $z = 0$. This is a diffusion equation with hydraulic
194 diffusivity $c = k/(\phi\beta\eta)$.

195 The evolution of plastic porosity can be viewed as a source/sink term. In the undrained
196 case, when compaction occurs, $\partial\phi_p/\partial t < 0$ and pore pressure increases; when dilation
197 occurs, $\partial\phi_p/\partial t > 0$ and pore pressure decreases.

198 2.3 Porosity Model

We adopt the Segall and Rice (1995) formulation of plastic porosity evolution and dilatancy. We recognize that some recent experiments such as Proctor et al. (2020) and Brantut (2020) exhibit more complex behaviors that cannot be captured by this formulation. However, as this remains the most widely used model for dilatancy within the earthquake modeling community, we believe it is the logical choice for a first step to incorporate porosity evolution in a fully coupled fluid-fault model. The formulation reads:

$$\frac{\partial \phi_p}{\partial t} = -\frac{V}{d_c}\left(\phi_p - \phi_{p,ss}(V)\right), \tag{15}$$

where the steady-state plastic porosity is

$$\phi_{p,ss}(V) = \phi_{p,0} + \epsilon \ln\frac{V}{V_0}, \tag{16}$$

199 where $\phi_{p,0}$ is the steady-state plastic porosity at reference velocity V_0 and ϵ is a dilatancy
200 coefficient, which experiments suggest is on the order of 10^{-4} (Segall & Rice, 1995).

The elastic component of porosity ϕ_e evolves according to the definition stated earlier:

$$\frac{\partial \phi_e}{\partial t} = \phi\beta_\phi\frac{\partial p}{\partial t}. \tag{17}$$

201 2.4 Permeability Model

Permeability evolution is intrinsically linked to the evolution of porous space. As pore connections are enhanced by dilation or the removal of fines along pore throats, permeability (and storage) are enhanced (Bernab et al., 2003). There is no one-to-one relationship between permeability and porosity applicable to all porous media, as the relation is very much dictated by the specific operating process, material, and microscopic pore structure. Nonetheless, a widely accepted permeability-porosity relationship is the generalized power law (Walder & Nur, 1984; Nelson, 1994; Zhu et al., 1995; Civan, 2001;

Luquot & Gouze, 2009; Menke et al., 2015; L. Zhang et al., 2015):

$$\frac{k}{k_0} = \left(\frac{\phi}{\phi_0}\right)^{\alpha}, \tag{18}$$

where k_0 and ϕ_0 are the reference permeability and porosity, and the exponent α has a wide range of values from 1 to 25, depending on the rock type and confining stress level. David et al. (1994), Bernab et al. (2003), and Johannes et al. (2018) have compiled some published data on the values of α for different materials and processes. Even for the same rock type and process, the value of α is far from unique. We have chosen $\alpha = 20$, at the higher end of observed values, but one that is consistent with experiments on certain types of sandstones (David et al., 1994). Lower values of α would result in less enhancement in permeability and fluid flow in response to porosity changes, while retaining the same dilatancy-induced suctions.

For the reference k_0, we have chosen 10^{-12} m^2, consistent with some recent in situ experiments (Guglielmi et al., 2015; Bhattacharya & Viesca, 2019; Larochelle et al., 2020), but perhaps on the higher end of fault zone permeability in basement rocks (Y. Zhang et al., 2013). The reference porosity ϕ_0 is chosen to be 10%, which is representative of fault gouges (Segall & Rice, 1995), and we have split this porosity equally into an elastic component and a plastic component for the purpose of modeling porosity separately in two ways.

3 Numerical Simulations

We have conducted a wide range of simulations to explore the effects of different initial state and prestress conditions, fluid injection rates, and frictional properties. We use a high-order SBP-SAT finite difference method for spatial discretization along with adaptive time stepping, with error control on slip and the state variable (Erickson & Dunham, 2014; Allison & Dunham, 2018; Duru et al., 2019). Pressure (14) and elastic porosity (17) are solved implicitly using backward Euler (using operator-splitting at the Runge-Kutta stage level), while slip (2), state variable (4), and plastic porosity (15) are solved explicitly an adaptive Runge-Kutta method (Zhu et al., 2020).

In the following sections, we have chosen to focus primarily on velocity-strengthening faults, as under upper crustal conditions and for temperatures less than 120°C, laboratory experiments have shown that gouges for characteristic lithologies associated with injection-induced seismicity (e.g., carbonates, shales, and organic-rich reservoir rocks) show predominantly velocity-strengthening behavior (Kohli & Zoback, 2013; Scuderi et al., 2017). Available data and studies also show that less than 2% of injection wells across the United States have been associated with induced earthquakes (Yehya et al., 2018), and evidence from some field sites suggests that a significant fraction of the induced slip and deformation is aseismic (Cornet et al., 1997; Evans et al., 2005; Zoback et al., 2012; Guglielmi et al., 2015; Duboeuf et al., 2017; Villiger et al., 2020). Results for velocity-weakening faults are presented at the end of Section 3.

Below, we list the parameters used in the simulations and explore the results systematically.

3.1 Parameters

The simulations use grid stretching in both the y and z directions, with finer grids near the injection site and sparser grids farther from there. The grid spacing within 2.5 km of the injection site is constant at 0.67 m, and farther from there stretches out according to a hyperbolic sine function. A critical length scale characterizing the process zone at the tip of a propagating rupture is $L_b = \mu d_c/\bar{\sigma}_n b$ (Dieterich, 1992; Ampuero & Rubin, 2008), at least for the aging state evolution law, with comparatively less known

for the slip law (Viesca, 2020). L_b is about 60 m in our set-up. Therefore, it is resolved by approximately 100 grid points near the injection site where the slip front initiates, and provides adequate resolution for the simulations. The parameters in Table 1 are the same across simulations except for the ones indicated as variable.

Symbol	Description	Value
Ly	Domain size in y direction	50 km
Lz	Domain size in z direction	50 km
μ	Shear modulus	32.4 GPa
d_c	Characteristic state evolution distance	1 mm
a	Rate-and-state direct effect parameter	0.01
b	Rate-and-state state evolution parameter	variable
τ_0	Initial shear stress	variable
Ψ_0	Initial state variable	variable
q_0	Fluid injection rate	variable
σ_n	Normal stress	50 MPa
V_0	Reference velocity	10^{-6} m/s
f_0	Reference friction coefficient	0.6
$\phi_{e,0}$	Reference elastic porosity	0.05
$\phi_{p,0}$	Reference plastic porosity	0.05
k_0	Reference permeability	10^{-12} m^2
α	Coefficient for porosity-permeability relation	20
ϵ	Dilatancy coefficient	2×10^{-4}
β_f	Fluid compressibility	0.55 GPa^{-1}
β_ϕ	Elastic pore compressibility	0.45 GPa^{-1}
η	Fluid viscosity	10^{-3} Pa s

Table 1. Reference parameters

3.2 Initial Conditions

We set a uniform prestress τ_0 and a uniform state variable Ψ_0 across the entire fault at $t = 0$. From these conditions, and the fact that stress changes from slip are zero, we determine the initial slip velocity on the fault by equating shear stress and frictional strength (3), and computing slip velocity using bracketed Newton's method (Kozdon et al., 2013).

We set the initial elastic porosity $\phi_{e,init} = 0.05$, but the initial plastic porosity is different depending on the initial slip velocity. For simplicity, we set the initial plastic porosity, $\phi_{p,init}$, to its steady state value at the initial slip velocity using (16) to compute the initial plastic porosity $\phi_{p,init}$. This value, added to the initial elastic porosity, gives the total initial porosity $\phi_{init} = \phi_{e,init} + \phi_{p,init}$.

The initial permeability is computed as $k_{init} = k_0(\phi_{init}/\phi_0)^\alpha$, where $\phi_0 = \phi_{e,0} + \phi_{p,0}$ is the reference total porosity, which is 0.1 here.

The higher τ_0 is, the higher the initial slip velocity, resulting in higher initial porosity and permeability. The opposite occurs for higher initial state Ψ_0. This is a result of the direct effect from rate-and-state friction. Figure 2 shows the relationship among these variables.

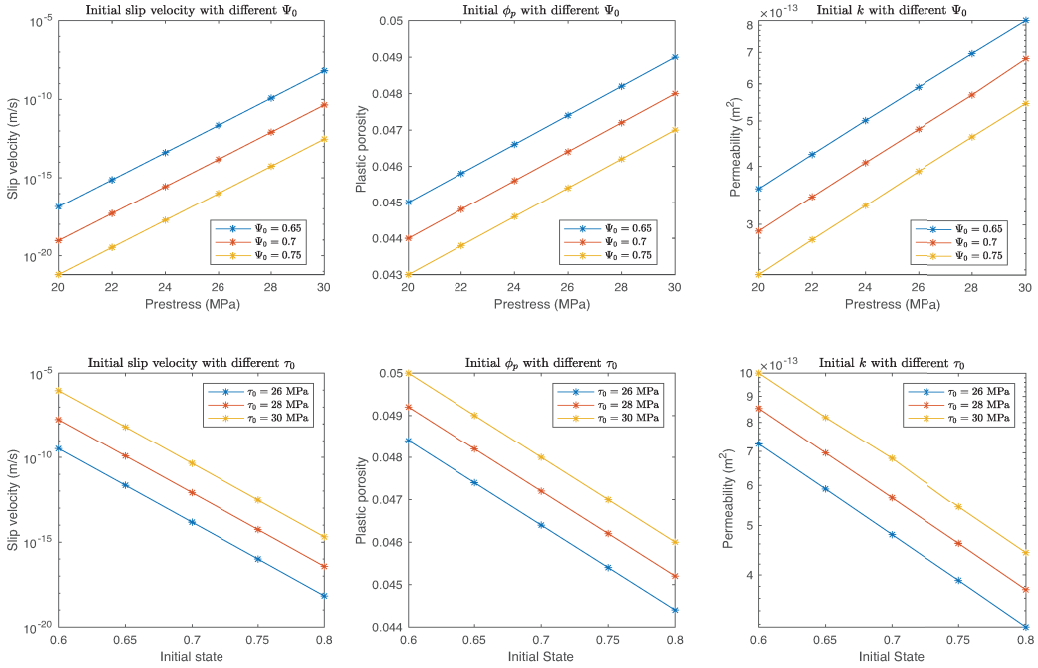

Figure 3. Fault response to fluid injection in the velocity-strengthening reference case. Space-

time plots of (a) slip velocity with pressure contours, (b) slip, (c) shear stress, (d) friction coefficient. There are two phases in the fault response to injection: an initial activation period with effectively linear diffusive pressurization, increasing friction coefficient, and negligible slip; followed by a second phase with constant-rate migration of aseismic slip that is driven by elastic stress transfer. Dilatant suction occurs at the slip front and causes pressure contours to propagate at constant rate during this second phase.

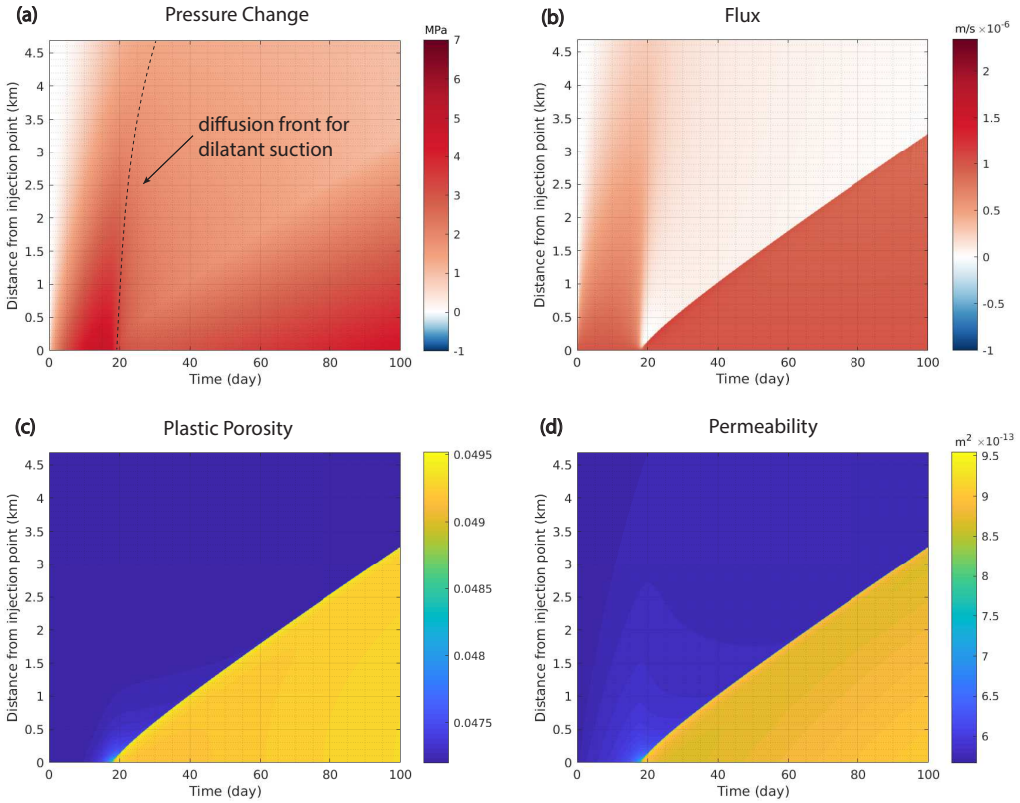

Figure 4. Fault response to fluid injection in the velocity-strengthening reference case. Space-time plots of (a) pressure change, (b) fluid flux, (c) plastic porosity, (d) permeability.

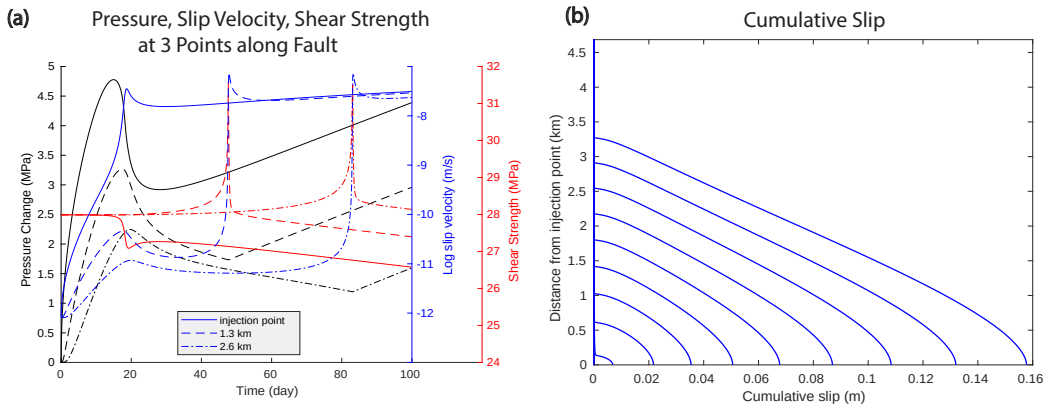

Figure 5. Fault response to fluid injection in the velocity-strengthening reference case. (a) Time series plot of pressure change (black), slip velocity (blue), and shear stress (red) at three points along the fault: $z = 0$, 1.3 km, and 2.6 km. (b) Cumulative slip plotted at 10-day intervals.

Figures 3 and 4 show the fault response to fluid injection. There are two phases to this response. The first phase is an activation period with negligible slip, during which

the pore pressure evolution is well approximated by a linear diffusion model (since dilatancy and changes in storage and permeability are negligible). Pressure at the injection site increases as the square-root of time, decreasing effective normal stress. Friction coefficient increases in response to the rate-and-state direct effect as effective normal stress decreases. During this phase, there is almost no change in shear stress, porosity, and permeability as slip and slip velocity are very small. The second phase is marked by the onset of significant crack expansion, where the aseismic slip front starts to propagate outward at constant rate. During this phase, significant dilatancy and a drop in pore pressure occur at the slip front. Pressure contours deviate from the linear diffusion model, due to dilatancy and other nonlinearities, and begin to propagate at a constant rate, although more slowly than the aseismic slip front. Also note that during the duration of the simulation, aseismic slip lags behind the commonly used $z = \sqrt{4\pi ct}$ prediction from linear pore pressure diffusion, where c is the hydraulic diffusivity (Shapiro et al., 1997; Shapiro & Dinske, 2009). However, the pore pressure contours in our model no longer follows linear diffusion due to the two-way coupling between fluid flow and fault slip.

We now discuss in more detail the first phase of the response to injection. The initial localized slip rate acceleration can be understood as a balance between the rate-and-state direct effect and the rate of change of effective normal stress near the injection site (Dublanchet, 2019). As the slip velocity is low ($< 10^{-9}$ m/s), dilatancy is negligible and changes in permeability and storage from the pressure-dependence of elastic porosity are also extremely small. Therefore, pore pressure diffusion (Figure 4a) is effectively linear. This is also evidenced by the 0.5 MPa and 2.5 MPa pressure contours in Figure 3a before 20 days, which advance in proportion to the square-root of time. Because slip is negligible in this first phase (Figure 3b), the shear stress remains effectively constant (Figure 3c). The direct effect causes the friction coefficient to increase as effective normal stress decreases at fixed shear stress (Figure 3d). This increases slip velocity to values between 10^{-8} and 10^{-7} m/s (Figure 3a). When slip becomes comparable to the state evolution distance (Figure 3b), friction begins to evolve toward a lower, steady state value. This frictional weakening leads to a stress drop that builds a stress concentration just outside a slipping patch around the injection site, initiating an outwardly propagating slip front about 20 days after the injection starts.

Now consider the second phase of the response, in which aseismic slip initiates near the injection site and migrates along the fault at a constant migration rate of about 35 m/day. At the start of this phase, around the injection site, slip velocity increases to about 10^{-7} m/s, increasing plastic porosity. This increases permeability (and, to a lesser extent, storage) but causes dilatant strengthening by reducing pore pressure (Figure 4c,d). However, permeability is only increased by about 50%. Even though this enhances fluid flow and pressure diffusion along the fault, the effect is secondary as compared to dilatant strengthening. At the onset of significant slip around 20 days, dilatancy near the injection site causes a substantial reduction in pressure as the fluid expands into newly dilated pore space. This suction near the injection site triggers a diffusive pressure reduction response that expands outward along the fault (Figure 4a), reducing fluid flux to nearly zero (Figure 4b). We have drawn a $z = \sqrt{4\pi ct}$ contour in Figure 4a to mark the diffusive response to dilatant suction, which advances across the fault in a few days, consistent with the predicted hydraulic diffusion time. Away from the injection site, pressure continues to decrease gradually and other conditions on the fault remain relatively constant until the arrival of the slip front.

Dilatancy at the slip front reduces pressure (Figure 4a) and suppresses further acceleration of the slip front, despite mild enhancement of permeability. Pressure diffusion in this second phase departs substantially from linear pore pressure diffusion due to dilatancy and the two-way coupling between slip and pressure changes. Pore pressure contours in this phase migrate at a constant rate that is slower than the migration rate of the aseismic slip front. We also note that fluid flux increases abruptly from nearly zero

at the slip front to a relatively constant value within the slipping part of the fault behind the slip front (Figure 4b).

A central question here is, what drives the aseismic slip front? We first note the shear stress concentration at the slip front (Figure 3c), similar to that at the tip of a shear crack. The friction coefficient decreases with state evolution toward a relatively constant value behind the slip front, leading to stress drop and slip behind the slip front. Continued injection leads to additional pressurization of the slipping portion of the fault, at relatively constant friction coefficient, causing additional stress drop and slip. We speculate that elastic stress transfer from slip in this central region provides the loading that drives the aseismic slip front.

Figure 5a provides an alternative view of these effects by showing time series of pressure, slip velocity, and shear stress at three locations along the fault. At all locations, pressure initially rises as the square-root of time during the first phase, consistent with the linear diffusion model prediction, before dropping during the diffusive response to dilatancy near the injection site at the start of the second phase. Then the slip front begins to propagate outward. Pressure reaches a minimum value at the slip front, and then begins to increase at an almost constant rate with the onset of slip and fluid flux. This repressurization, and gradual drop in shear stress, occurs because the fluid delivered by the sustained injection cannot be fully accommodated by the dilated pore space. All of these features, taken together, suggests that injection pressurizes the fault interior, causing stress drop and slip, which through elastic stress transfer maintains the stress concentration at the migrating slip front.

Figure 5b shows the cumulative slip over 100 days along the fault, with each successive line spaced 10 days apart. The largest slip occurs at the injection point. Over 100 days, the center of the fault has accumulated 0.16 m of slip, which translates to an average slip velocity of about 2×10^{-8} m/s. This large amount of slip, if occurring on a sufficiently shallow fault, should be detectable with geodetic observations as well as deformation or even shear failure of the casing in wells that cross the fault.

3.4 No Porosity or Permeability Evolution (One-Way Coupling)

Having presented and explained the solution from our fully coupled model that accounts for porosity and permeability evolution, we now discuss how ignoring porosity and permeability evolution impacts the nature of the solution. In this section, we consider the slip response to linear pore pressure diffusion, with one-way coupling from pore pressure changes to fault slip through changes in effective stress and shear strength. This one-way coupling approach has been widely used in recent studies (Bhattacharya & Viesca, 2019; Dublanchet, 2019). In fact, the simulation set-up in this section is identical to that in Dublanchet (2019), except for our use of the slip law instead of the aging law for state evolution. Results are summarized in Figure 6. As in our previous model, there are two phases of the fault response to injection. The first phase has negligible slip and shear stress change, with accelerating slip velocity near the injection site bringing the fault toward instability. The second phase features the outward migration of an aseismic slip front. Consistent with Dublanchet (2019), the slip front advances beyond the (linear diffusion) pressure contours. Despite these general similarities with our previous simulations, there are substantial quantitative differences. First, outward slip migration is triggered much earlier, at about 8 days as compared to 20 days in the previous case. The peak slip velocity at the slip front is very high ($\sim 10^{-4}$ m/s, about two orders of magnitude higher than in our previous model with dilatancy). Moreover, the migration rate is 400 m/day, over ten times higher than in our previous model. All of these difference contribute to much larger slip; slip at the injection point reaches almost 0.9 m after just 20 days. Therefore, we conclude that the dilatant strengthening effect is very significant and drastically changes the nature of the resulting slip.

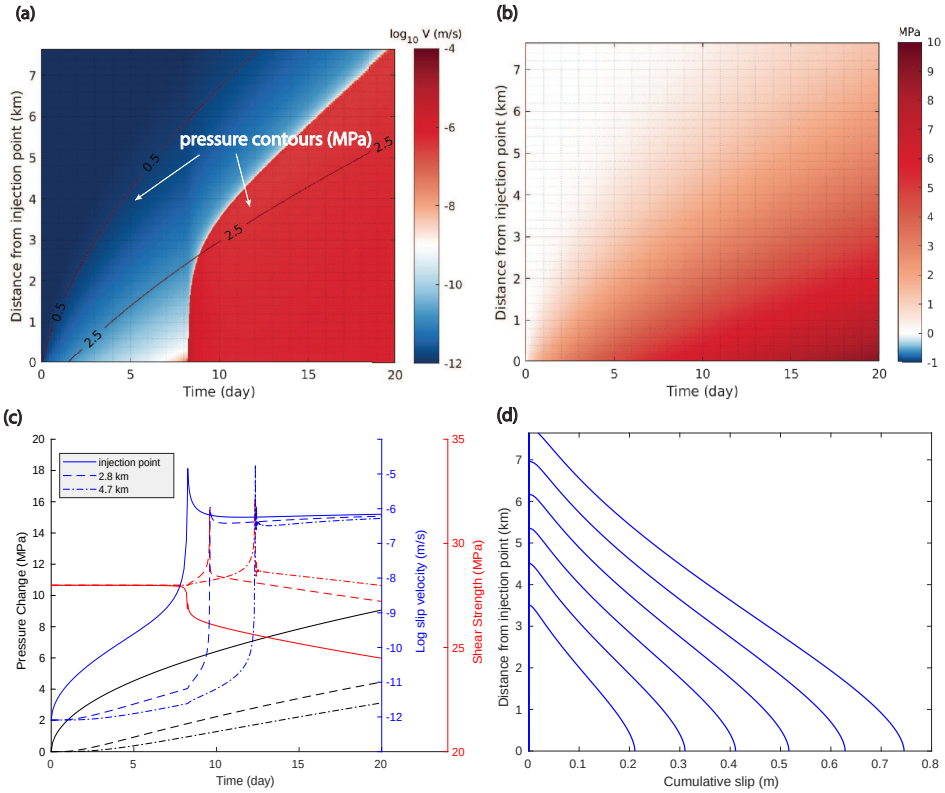

Figure 6. Fault response to fluid injection in the velocity-strengthening reference case, but neglecting porosity and permeability evolution. Space-time plots of (a) slip velocity and (b) pressure change. (c) Time series of pressure change (black), slip velocity (blue), and shear stress (red) at three points along the fault: $z = 0$, 2.8 km ,and 4.7 km. (d) Cumulative slip plotted at 2-day intervals. Slip is much larger, is triggered earlier, and migrates at a much faster rate than in the model accounting for porosity and permeability evolution (Figures 3–5).

3.5 Effect of Prestress

In this and the following sections we return to models accounting for porosity and permeability evolution, but vary several model parameters to explore controls on the fault response. Here, we vary the prestress τ_0. We discuss results in terms of the closeness-to-failure ratio:

$$CTF = \frac{\tau_0}{f_0(\sigma_0 - p_0)}. \tag{19}$$

The closer CTF is to unity, the closer the fault is to failure. This ratio plays a central role in the fluid injection studies of Bhattacharya and Viesca (2019) and Wynants-Morel et al. (2020). Moreover, CTF is a useful means of quantifying the pressure perturbation that is required to initiate slip on a fault obeying a Mohr-Coulomb failure criterion (Norbeck & Horne, 2018). Figure 7 shows results for $\tau_0 = 26$, 28, and 30 MPa, which correspond to $CTF = 0.867$, 0.933, and 1.

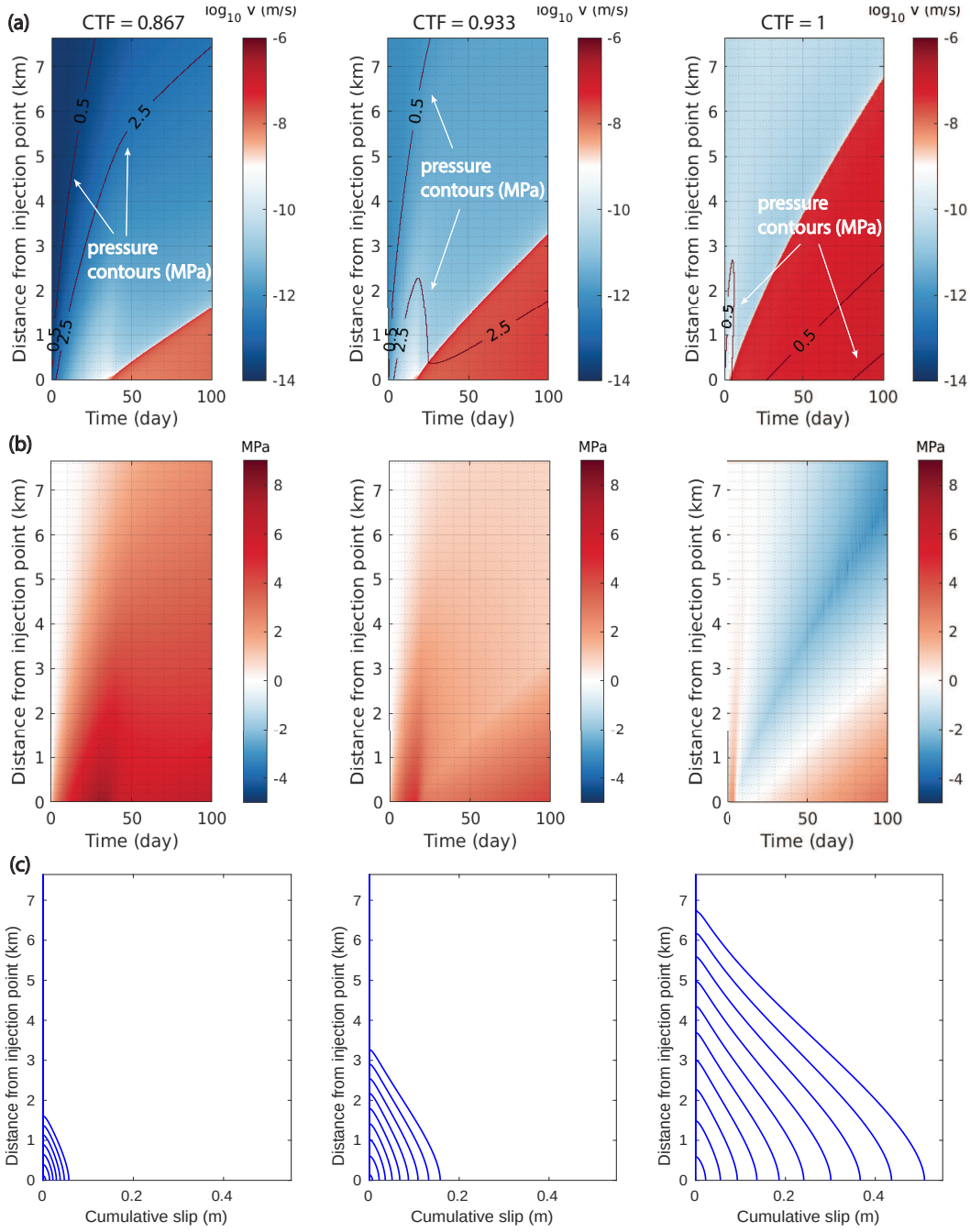

Figure 7. Space-time plots of (a) slip velocity and (b) pressure change, and (c) cumulative slip at 10-day intervals, for $CTF = 0.867$, 0.933, and 1 from left to right. Higher CTF leads to faster migration rates of the aseismic slip front, despite stronger dilatancy. Cumulative slip also increases with CTF.

Our reference case discussed in Section 3.3 is the middle panel in Figure 7. On the left and right are cases with lower and higher prestress, respectively. First, the closer the fault is to failure, the earlier significant aseismic slip is triggered. With $CTF = 0.867$, aseismic slip with velocity greater than 10^{-9} m/s is only triggered at around 40 days, whereas for $CTF = 0.933$, it is triggered at 20 days, and for $CTF = 1$, 5 days. Sec-

ond, the slip front migration rate increases with increasing τ_0. This is not surprising given that higher τ_0 means higher CTF and also larger stress drop, providing more strain energy to drive the expanding slip front. Even though dilatancy is greater for a higher τ_0, it is does not counteract the additional stress drop. Delayed triggering and lower slip rate for lower prestress conditions is also observed in experimental studies such as Scuderi et al. (2017).

It is also notable that pressure diffusion in the beginning is a lot faster than slip front propagation for lower τ_0, as dilatancy is weaker. The difference is quite pronounced across the cases examined here when we look at the 0.5 MPa and 2.5 MPa contours in Figure 7a. Going to higher τ_0, the aseismic slip front outpaces the pore pressure contours much sooner and their gap becomes much wider. In Figure 7b we can see that the pressure change even becomes negative for $CTF = 1$ due to the high slip velocity creating very strong dilatant suctions. Therefore, taking dilatancy into account with our current formulation has two implications. First, there is an initial period of time over which dilatancy has not had a significant impact yet and the slip front lags behind the pressure contours. Second, in faults closer to failure, the aseismic slip front overtakes the pore pressure diffusion earlier.

Finally, Figure 7c shows the cumulative slip. Increasing CTF makes a large difference in the total slip. Therefore, understanding the prestress condition of a fault before injection has important implications on the potential amount of slip that can be triggered.

3.6 Effect of Initial State

Next we consider the influence of the initial state variable Ψ_0. With other initial conditions and parameters fixed, higher Ψ_0 results in a lower initial velocity (Figure 2). Therefore we anticipate that the trend here would be the opposite of that discussed in the previous section, and indeed, we see in Figure 8 that increasing Ψ_0 results in aseismic slip being triggered at later times and slower slip front migration rates. In all three cases, the maximum slip velocity reached is about the same, therefore the dilatancy effect approximately the same, in contrast to the large differences seen when we alter the prestress. The total slip increases for lower Ψ_0.

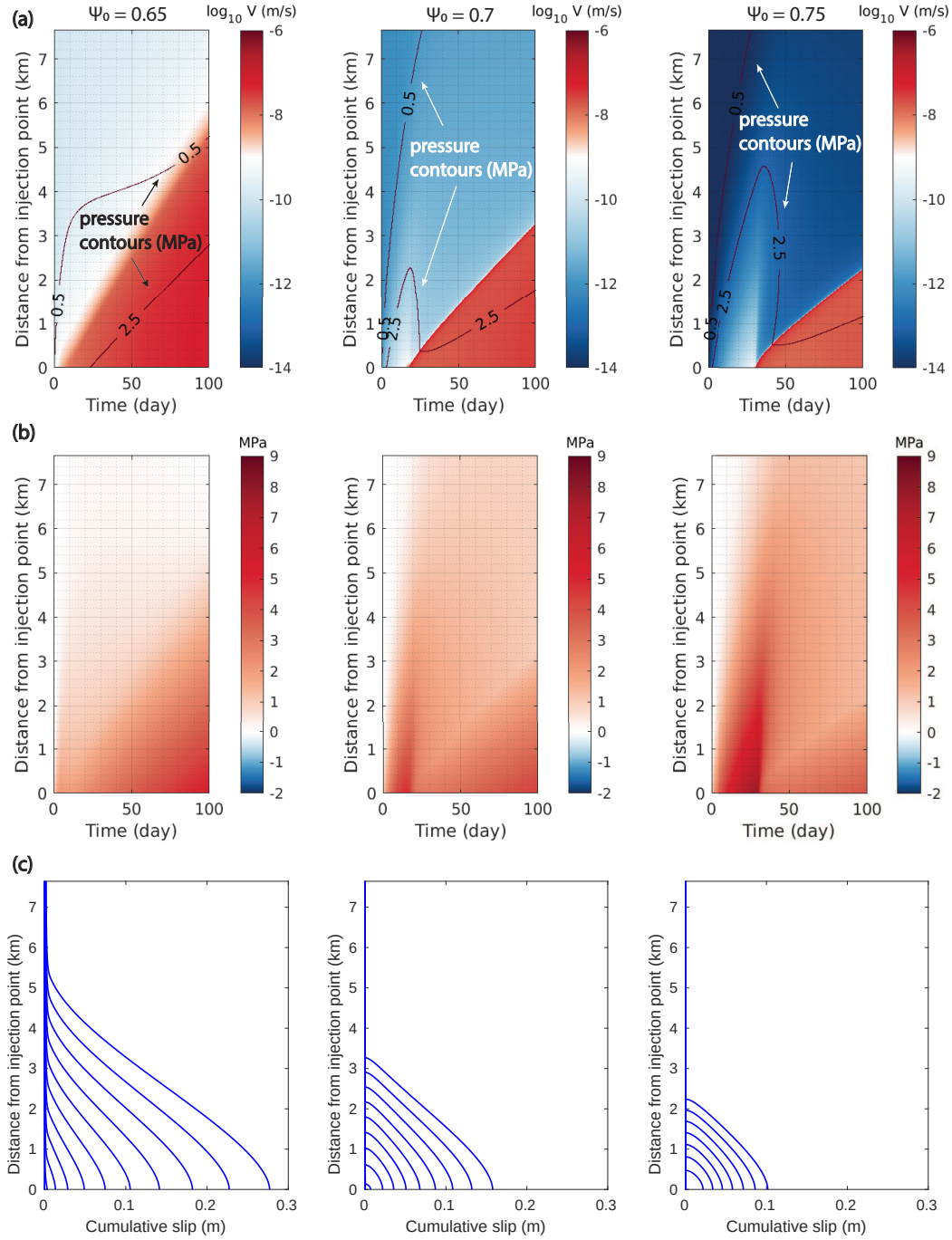

Figure 8. Space-time plot of (a) slip velocity and (b) pressure change, and (c) cumulative slip at 10-day intervals, for Ψ_0 = 0.65, 0.7, 0.75 from left to right. The higher Ψ_0 is, the slower the aseismic slip front propagation.

3.7 Effect of Injection Rate

We now examine the effect of the injection rate. Figure 9 shows the slip velocity and pressure change for $q_0 = 10^{-6}$, 2×10^{-6}, and 4×10^{-6} m/s. Higher injection rates trigger slip earlier. Slip velocity is also higher and the slip front propagates faster. Even though dilatancy is stronger for higher injection rates, the elastic stress transfer due to

larger stress drop as a result of higher pore pressure perturbations is the dominant effect. The slip front takes less time to outpace the pore pressure contours for higher injection rates. Furthermore, as the injection rate doubles, the total amount of slip grows significantly. With $q_0 = 10^{-6}$ m/s, the slip over 100 days is less than 3 cm, but it grows to close to 20 cm for $q_0 = 2 \times 10^{-6}$ m/s and 80 cm for $q_0 = 4 \times 10^{-6}$ m/s. However, when we consider the same total injected volume, the amount of slip is in fact not that different across the different injection rates. The slip over 100 days for $q_0 = 10^{-6}$ m/s is slightly lower than the slip over 50 days for $q_0 = 2 \times 10^{-6}$ m/s, which is about the same as the slip over 25 days for $q_0 = 4 \times 10^{-6}$ m/s. These are marked in red in Figure 9c. Nevertheless, as higher injection rate is able to trigger significant amounts of slip earlier, in actual injection operations, it is a major risk factor to control. Similar conclusions regarding the importance of pressurization rate have also been reached in some experimental (L. Wang et al., 2020) and modeling (Alghannam & Juanes, 2020) studies.

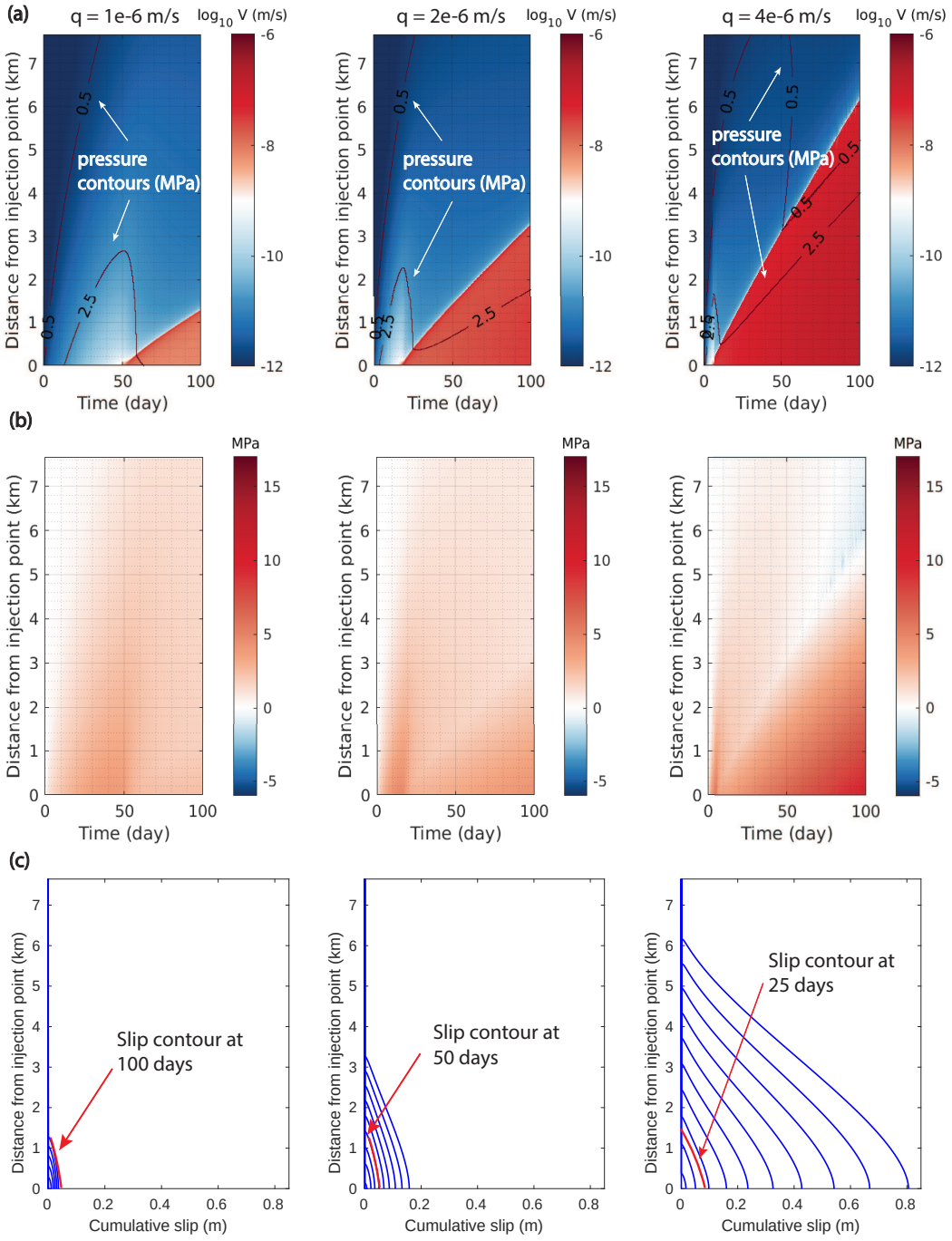

Figure 9. Space-time plots of (a) slip velocity and (b) pressure change, and (c) cumulative slip at 10-day intervals, for different injection rates $q_0 = 10^{-6}$, 2×10^{-6} and 4×10^{-6} m/s. The higher the injection rate, the higher the slip velocity, and the faster the aseismic slip front propagates. Total slip also increases dramatically if one considers the same injection time. Red slip contours in (c) indicate times when the total injected volume is identical across all simulations, highlighting that the total slip for the same injected volume is similar.

In Figure 10, we quantify migration rates of the aseismic slip front and the 2.5 MPa pore pressure contour as a function of injection rate q_0. In fact, we see that for higher

injection rates, the 0.5 MPa contour also comes down due to stronger dilatancy effect and travels at the same speed as the 2.5 MPa contour. The migration rate is measured as the steady state value that is reached and sustained at later times. Fitting the curves to a power-law function of q_0 shows a close match. The fitting functions are $1.725\times10^6{q_0}^{0.8139}$ for the aseismic slip front and $1.8 \times 10^6{q_0}^{0.864}$ for the pore pressure contours (for migration rate and q_0 in m/day).

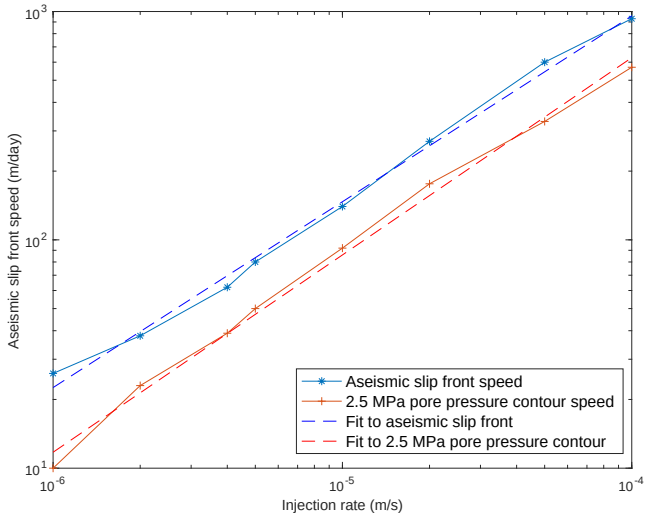

Figure 10. Steady state migration rates of aseismic slip front (blue) and 2.5 MPa pore pressure contour (red) for different injection rates q_0. Power-law fits are plotted in dotted lines.

3.8 Effect of Frictional Properties

Finally, we examine the influence of frictional properties. In Figure 11, we show the comparison plots for $a-b = 0.001$, 0.005 and 0.01 with $a = 0.01$ held fixed. Overall, the changes in aseismic slip front migration rate and the total amount of slip from varying $a-$ are much smaller than when other model parameters are varied, although there are some subtle differences. The differences arise from differences in residual friction behind the slip front, which decreases as $a-b$ increases (because slip velocities are less than the reference velocity V_0 at which steady state friction equals f_0). This causes slip to initiate slightly earlier and leads to somewhat faster migration rates of the slip front for larger $a-b$. Figure 12 shows more details of the time evolution of friction coefficient at the injection point.

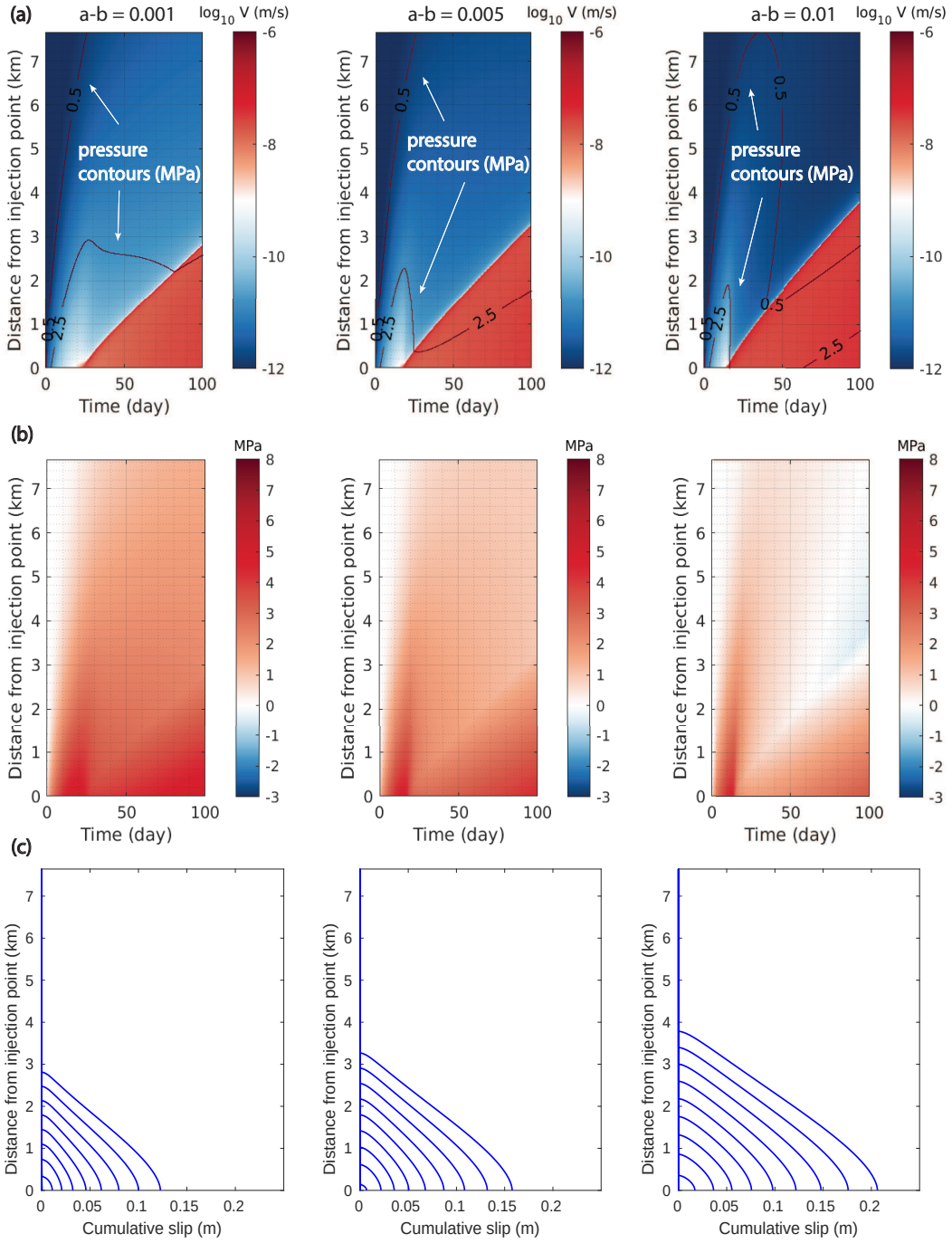

Figure 11. Space-time plots of (a) slip velocity and (b) pressure change, and (c) cumulative slip at 10-day intervals, for $a - b = 0.001$, 0.005 and 0.01, with $a = 0.01$ held fixed. Overall, changes in $a - b$ produce only minor differences in the solution.

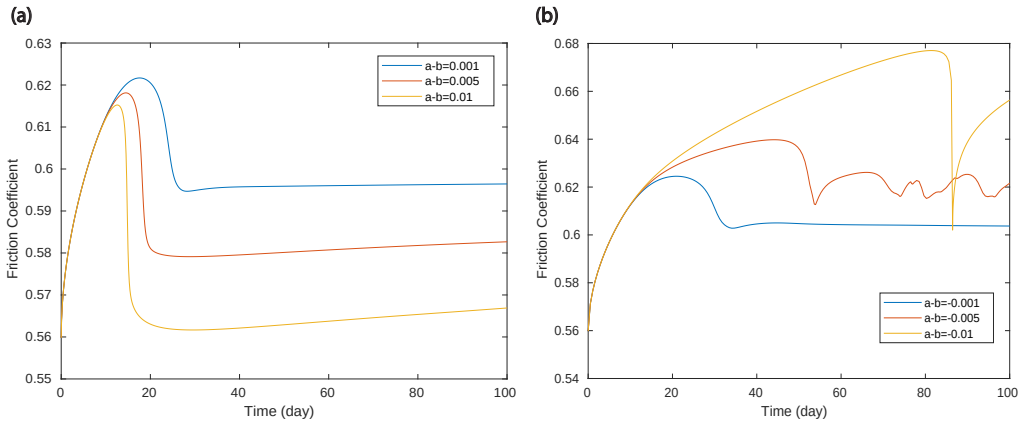

Figure 12. Friction coefficient at the injection point for different (a) velocity-strengthening and (b) velocity-weakening properties.

3.9 Velocity-weakening Fault

Thus far we have examined only velocity-strengthening faults. Here we explore velocity-weakening faults, starting with a reference case that is identical to the reference velocity-strengthening case (Figures 3–5) except with $a - b = -0.005$. For velocity-weakening friction, we do not present a comparison for different prestress, initial state variable, or frictional properties, as they show similar trends to the velocity-strengthening case. However, we do study the influence of injection rate.

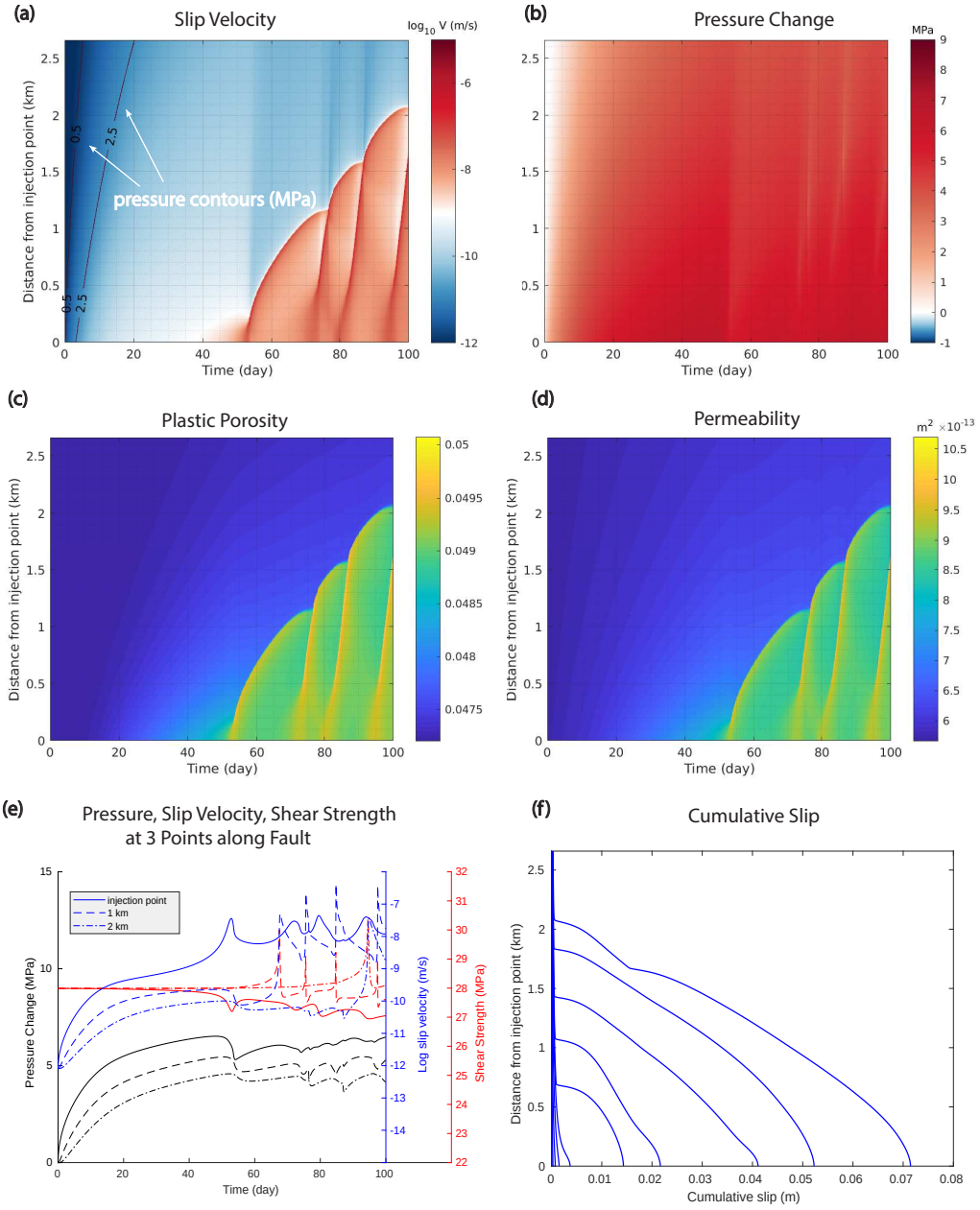

Figure 13. Fault response to fluid injection with velocity-weakening friction ($a - b = -0.005$). Space-time plots of (a) Slip velocity, (b) pressure change, (c) plastic porosity, and (d) permeability. (e) Time series of pressure change (black), slip velocity (blue), and shear strength (red) at three points along the fault: $z = 0$, 1 km, and 2 km. (f) Cumulative slip plotted at 10-day intervals. Velocity-weakening friction leads to spontaneously forming slip pulses instead of a single slip front migrating at constant rate as in the velocity-strengthening case. Triggering of slip is also delayed.

The slip behavior for velocity-weakening friction is quite different from the velocity-strengthening case. Rather than a single slip front migrating outward at a constant rate, fluid injection drives multiple slip pulses that are spontaneously generated at the injection site. These slip pulses successively advance on the previously slipped part of the fault,

incrementally advancing the overall slip front. Each slip pulse has its own front featuring concentrations in stress and slip velocity (Figure 13a), and behind these fronts the slip velocity drops by over an order of magnitude. This translates to dilation and permeability enhancement at the slip pulse fronts but compaction and healing inside (Figure 13c-d). Because the maximum slip velocity is about an order of magnitude higher than in the velocity-strengthening case (compare Figures 3a and 13a), dilatancy is also more substantial. This is most evident in the pressure time series plots (compare Figures 5a and 13e).

As we increase the injection rate, these slip pulses become more and more closely spaced in time (Figure 14). At sufficiently high injection rate, the individual slip pulses merge together, and the overall aseismic slip front migrates at a constant rate as in a velocity-strengthening fault. We speculate that after the initiation of each slip pulse, the interior of the slipped region has reached almost steady sliding conditions which are unstable to pore pressure perturbations, therefore causing the generation of ensuing slip pulses. As the injection rate increases, such perturbations become large enough so that these slip pulses are generated faster and eventually become rather indistinguishable. A linear stability analysis is needed to further quantify this phenomenon.

Slip is triggered at around 50 days for the reference velocity-weakening case, far later than the 20 days triggering time for the velocity-strengthening case (compare Figures 3a and 13a). This is because the residual friction coefficient is smaller for velocity-strengthening friction than for velocity-weakening friction, at the low slip velocities occurring within the aseismic slip region (compare to results in Section 3.8; see also Figure 12).

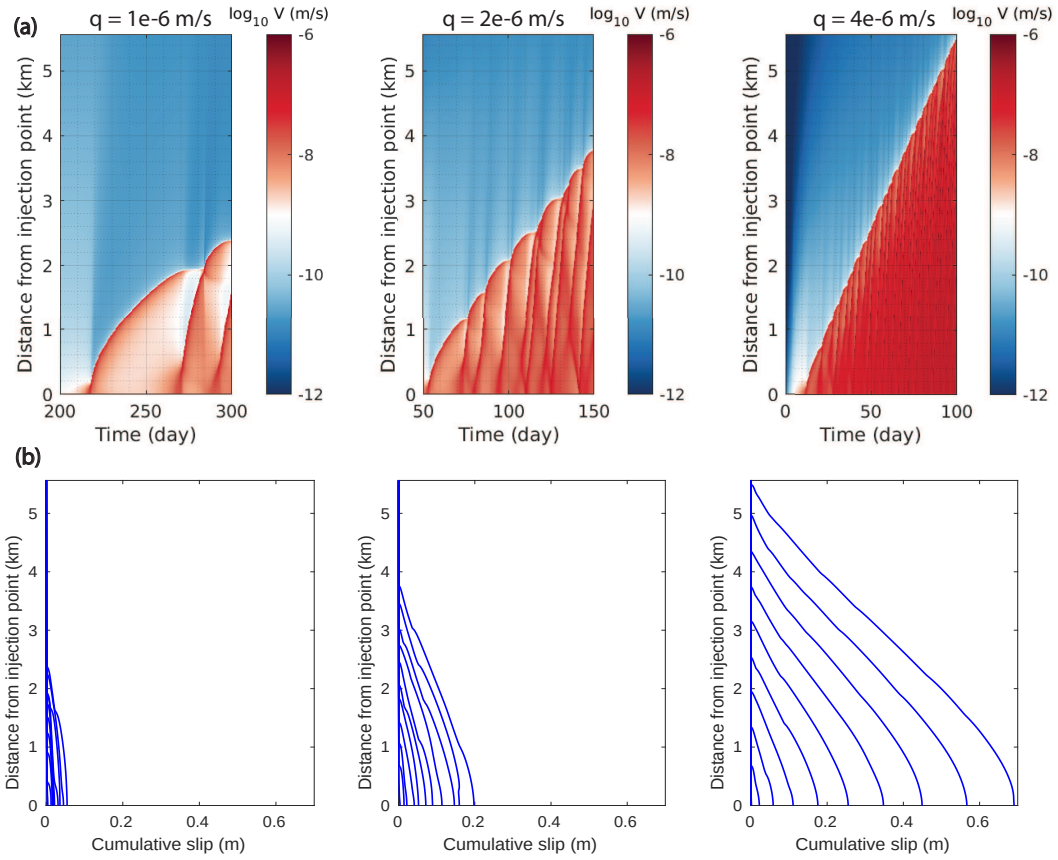

Figure 14. (a) Space-time plot of slip velocity for the reference velocity-weakening fault while varying the injection rate. From left to right, $q_0 = 10^{-6}$, 2×10^{-6} and 4×10^{-6} m/s. Shown for 100 days in all cases, but starting when the slip front begins migrating. As injection rate increases, individual slip pulses merge into a single slip front migrating at constant rate. (b) Cumulative slip at 10-day intervals. Total slip is comparable to the velocity-strengthening cases in Figure 9c.

Finally, if we neglect porosity and permeability evolution for the reference velocity-weakening fault, an earthquake nucleates and ends up rupturing the entire fault (not shown). This highlights the importance of the stabilizing effect of dilatancy, which in some cases may prevent seismic rupture in response to fluid injection.

4 Discussion

In this section, we first compare our study with previous work involving one-way coupling between pore pressure and slip, highlighting the importance of dilatancy. After that, we turn to several observational studies of seismicity triggered by fluid injection, comparing the aseismic slip migration rate predicted by our model to observed seismicity patterns. Finally, we discuss some limitations of our model and suggest future improvements.

4.1 Comparison to Models with One-Way Coupling From Pore Pressure to Slip

Many studies of induced seismicity utilize a one-way coupling from linear pore pressure diffusion to fault slip (Dieterich et al., 2015; Bhattacharya & Viesca, 2019; Dublanchet, 2019; Larochelle et al., 2020), thereby neglecting nonlinearities such as dilatancy. How does this impact model predictions? The closest modeling study to ours is by Dublanchet (2019); the 2D model set-up of injection into a fault is identical, except that we use the slip law instead of the aging law. We also account for two-way coupling between porosity, permeability, pore pressure, and slip, whereas Dublanchet (2019) uses a linear pore pressure diffusion solution that is one-way coupled to slip. The model of Dublanchet (2019) predicts constant-rate migration of an aseismic slip front when starting from below steady state, which he argues is the most probable scenario on real faults. Our model also predicts constant-rate aseismic slip front migration, but at a much slower rate. However, for a fault initially above steady state, we do not observe an accelerating aseismic slip front similar to the nucleation of a dynamic rupture, at least for the range of parameters we explored.

The coupling between slip velocity and porosity in our model produces significant dilatancy that strengthens the fault and inhibits further destabilization. Dilatancy not only changes the slip pattern on the fault, but it also alters the pore pressure diffusion pattern, bringing about a more complex relation between the migration speeds of aseismic slip and pore pressure contours. Various observations might be able to distinguish between the linear pore pressure diffusion model and our coupled model, for example, measuring pressure and slip in monitoring wells that are hydraulically connected to the fault. In comparison, when porosity and permeability evolution are neglected, as in Dublanchet (2019), fault slip begins much sooner, with a higher maximum slip velocity, much faster aseismic slip front migration, and a few hundred times more total slip, approaching values that seem implausible. For a velocity-weakening fault, the contrast of results is even greater. The system transitions from aseismic slip to seismic rupture when the stabilizing effects of dilatancy are neglected, whereas we find that dilatancy stabilizes slip and leads to complex aseismic slip patterns involving multiple active slip pulses. Overall, these results demonstrate that dilatancy can radically change the slip response to injection.

4.2 Connections to Experiments

Our results echo similar conclusions reached by many experimental studies. Lockner and Byerlee (1994) demonstrated that dilatancy can suppress shear localization and favor distributed shear, likely producing aseismic slip rather than earthquakes. Samuelson et al. (2009) noted that shear-induced dilatancy could be of sufficient magnitude to depressurize pore fluid and inhibit seismic rupture nucleation or propagation. Brantut (2020) discussed how the roughness of spontaneously formed faults plays a key role in producing strong dilatancy. Results from these studies are generally in agreement with the stabilizing effect we observe in our simulations. However, dilatancy has not often been emphasized sufficiently in numerical simulations that seek to characterize mechanisms of induced seismicity. We believe that this study could serve as a guide for future work that integrates essential physical processes to examine injection-induced fault slip. That said, there is considerable variability in the experimentally observed porosity and pressure response to slip, with some experiments even showing pressurization from compaction rather than suctions from dilatancy (Proctor et al., 2020). Future modeling studies should explore the compaction limit as well, by changing the sign of the dilatancy parameter ϵ.

4.3 Comparison to Observations

Our model makes several predictions that can be used for validation purposes, such as the migration rate of the aseismic slip front and slip. Our model predicts slip of a few

centimeters for the lower injection rates we explored, which is consistent with some borehole observations of centimeter-scale aseismic slip in fluid-injection experiments (Cornet et al., 1997; Evans, 2001; Guglielmi et al., 2015). Our model also predicts strains surrounding the fault that might be compared to measurements using fiber optic distributed acoustic sensing (?, ?, ?). Additionally, the predicted migration rate of aseismic slip ranges from about 50 to 1000 m/day, depending on the injection rate. There are few direct observations of injection-induced aseismic slip, but many believe that microseismicity, arising from small seismogenic patches within an otherwise aseismically slipping fault, tracks aseismic slip (Dublanchet et al., 2013; Jiang & Lapusta, 2016, 2017; Wynants-Morel et al., 2020). This connection is supported by modeling studies employing a heterogeneous mixture of frictional properties, particularly $a - b$ (Lui & Lapusta, 2016; Luo & Ampuero, 2018; Dublanchet, 2018; Almakari et al., 2019).

Microseismicity patterns from injection have three general patterns: diffusive, constant rate, and no pattern (Goebel & Brodsky, 2018). Examples of constant-rate migration include the 20032004 Corinth Gulf swarm in Greece (Duverger et al., 2015), in which the seismic swarm migrated horizontally over 10 km at an average rate of 50 m/day. Similar patterns were also observed at the Rittershoffen geothermal site in France (Lengliné et al., 2017), where the average migration rate of seismicity was about 300 m/day. Another example is the injection stimulation operation for an enhanced geothermal system project underneath Basel, Switzerland, in 2006. The targeted injection zone consisted of a fractured granite, which showed evidence for preexisting fracture zones and faults with relatively high transmissivity (Goebel & Brodsky, 2018). Injection lasted for 6 days with a total injected volume of 11,570 m^3 (Häring et al., 2008). While the injection rate was gradually increased, the average rate was $q_0 \approx 2.2 \times 10^{-6}$ m/s, assuming a total area of 10^4 m^2 through which the fluid diffuses (the same as assumed in our model). Using the reference velocity-strengthening case conditions, we predict an aseismic slip migration rate of about 50 m/day for this q_0. This is remarkably close to the migration rate of about 70 m/day obtained by a linear fit to microseismicity data (Goebel & Brodsky, 2018). A final example is a long-lasting swarm from 2016-2019 near Cahuilla, California, which may have been triggered by the release of a deep, natural fluid source (Ross et al., 2020). The migration speeds of microseismic events are very slow, about 1-5 m/day. This would correspond to an injection rate of about 1.4×10^{-8}-1.1×10^{-7} m/s in our model, by extrapolation of results in Figure 10.

Other earthquake swarms show much faster migration rates, close to 1000 m/day (Shelly et al., 2013, 2016). Such speeds are only sustained for a few days before significant deceleration. Fluid discharge from volcanic sources generally occurs at rather low rates, but it is possible to have intermittent rupturing of permeability seals (Ross et al., 2020) which temporarily results in pulses of high rate flow. This could trigger aseismic slip that migrates at the observed high rates for a short period of time.

4.4 Model Limitations

Arguably the most severe approximation in our study is the neglect of fault-normal fluid flow. Fault-normal flow can reduce or even mitigate dilatancy-induced suctions as fluids are drawn in the newly created pore space from the fault zone bordering the slip surface. This process has been examined using a fault-normal pore pressure diffusion model in Segall et al. (2010). The most nature extension of our model would be to account for fluid flow in both the along-fault and fault-normal directions, or even to generalize to full poroelasticity. Based on comparisons between behavior with and without dilatancy, we anticipate that accounting for fault-normal flow will increase the migration rate of aseismic slip fronts as well as the total slip.

In addition, the porosity evolution model we used assumes a positive relation between slip rate and steady state porosity (i.e., shear-induced dilation), but some exper-

imental studies provide evidence of shear-enhanced compaction (Tanikawa et al., 2012; Faulkner et al., 2018; Proctor et al., 2020). Compaction will pressurize the fault further and can even trigger dynamic instability on velocity-strengthening faults (Scuderi et al., 2017). Some modeling studies have examined how shear-induced compaction triggered by the large stress concentrations ahead of a propagating rupture can rapidly elevate pore pressure and weaken the fault surface, promoting rupture propagation (Hirakawa & Ma, 2016). There is presently little understanding of the conditions that determine whether faults will dilate or compact under shear deformation. Some argue that dilatancy would be most pronounced for shearing of relatively intact rocks or faults that slip after long dormant periods during healing and sealing processes (Brantut, 2020). On the other hand, there is also the argument that the comminution effect, and the production of wear products from fracture surfaces, are mostly dominant during initial shear-in on artificial fresh surfaces and for short healing/sealing periods, which may not be broadly representative of natural systems (Im et al., 2018). We can conclude from these varied observations that porosity evolution with slip is complex and dependent on the initial state of the fault zone and how shearing is accommodated within the fault zone. Further experimental work is needed to better quantify the relation among porosity, slip, and other relevant mechanical and hydrological parameters under different faulting conditions.

Moreover, the evolution of permeability with porosity is also subject to much variability. There could be cases where permeability increases due to pore connectivity enhancement without an actual increase in porosity, as captured through the tortuosity parameter in the Kozeny-Carman relation (Bernab et al., 2003). Some recent studies focus on this limit, and couple permeability with both effective normal stress and slip while neglecting changes in porosity and storage (Zhu et al., 2020). Furthermore, the power-law relation between porosity and permeability used in this study also does not have a fixed exponent for all processes and rock types (David et al., 1994), nor is it even clear if a power-law relation is relevant in all cases. These relations and associated parameters are likely dependent on the specific formation or tectonic history of the region, arguing for experimental characterization of fluid transport properties from core samples when numerical simulations are used for induced seismicity hazard studies. Moreover, recent efforts to develop and utilize borehole instrumentation packages to measure pore pressure, slip, and other conditions offer the exciting promise of better constraints to validate models of fluid-induced aseismic slip (Guglielmi et al., 2015; Savage et al., 2017).

Finally, some studies also suggest that fault frictional properties evolve during fluid injection, thereby influencing the resulting slip. Cappa et al. (2019) showed that faults can undergo a transition from velocity weakening to velocity strengthening with increasing fluid pressure above slip velocities of about 10 mm/s. Scuderi et al. (2017) also observed that the increase of fluid pressure influences the evolution of the rate-and-state friction parameters and consequently the critical nucleation length. Additionally, some experiments suggest that pore pressure may alter fault strength in a manner that is more complex than just through the Terzaghi effective stress (French et al., 2016). Our model has assumed constant rate-and-state parameters for the fault and the standard Terzaghi effective stress model, but in actuality, fluid injection and pressurization may create more complex changes than can be captured through our model framework. Future work is needed to better understand effects of pressurization on the frictional strength of faults.

5 Conclusion

In this study, we have modeled the aseismic slip resulting from fluid injection in a 2D rate-and-state fault coupled with porosity and permeability evolution. Constant rate fluid injection into the fault predicts steadily propagating aseismic slip front lags behind the linear pressure diffusion prediction of $z = \sqrt{4\pi ct}$. However, dilatancy from slip alters pore pressure diffusion, such that pore pressure contours migrate at a constant

rate that is slower than the aseismic slip front. From our simulation results, we gain the following insights:

1. The evolution of porosity and permeability influences both slip and pore pressure diffusion.
2. Increasing prestress increases the slip velocity and the migration rate of aseismic slip. This is because the higher stress drop dominates over a stronger dilatancy effect.
3. Decreasing the initial state variable increases the slip velocity and the migration rate of aseismic slip. Dilatancy is approximately the same.
4. Injection rate, which is the most controllable variable in actual injection operations, has a very significant impact on the resulting slip. Lower injection rates delay the triggering of slip and causes it to migrate at a slower rater. Slip accumulates at a lower rate, but the total amount of slip is approximately the same when the same volume of fluid is injected at different rates. Dilatancy is weaker for lower injection rates.
5. Changing $a-b$ while keeping a constant causes only minor differences in the slip response. Because slip velocities are less than the reference slip velocity V_0, the overall friction coefficient is lower for more velocity strengthening or less velocity weakening faults, which makes the fault slip earlier and at a faster migration rate.

Overall, we note that nonlinearities in fluid transport, especially dilatancy, fundamentally alter the slip response to injection as compared to slip driven by linear pore pressure diffusion. In particular, dilatant strengthening prevents further acceleration of the aseismic slip front and, for the parameter choices explored in this study, suppresses the onset of seismic slip even in a velocity-weakening fault. In real faults, the evolution of porosity and permeability and their impact on fluid pathways, along with the geological structure of the fault and its surrounding damage zone, are much more complex than have been explored in this study. However, our simplified formulation is sufficient to demonstrate the importance of integrating these hydromechanical processes into numerical models, in order to gain a comprehensive understanding of the fluid-rock interaction in injection-induced slip.

Acknowledgments

This research was supported by the National Science Foundation (EAR-1947448) and the Southern California Earthquake Center (Contribution No. 10846). SCEC is funded by NSF Cooperative Agreement EAR-1600087 & USGS Cooperative Agreement G17AC00047. We thank Kali Allison and Weiqiang Zhu for assisting with code development. The source code is available at https://bitbucket.org/yyang85/scycle-2, where a list of input files used for this study is also provided. Data used to produce the figures can be found at DOI 10.17605/OSF.IO/TV2SX.

References

Alghannam, M., & Juanes, R. (2020). Understanding rate effects in injection-induced earthquakes. *Nature communications*, *11*(1), 1–6. doi: 10.1038/s41467-020-16860-y

Allison, K. L., & Dunham, E. M. (2018). Earthquake cycle simulations with rate-and-state friction and power-law viscoelasticity. *Tectonophysics*, *733*, 232–256. doi: 10.1016/j.tecto.2017.10.021

Almakari, M., Dublanchet, P., Chauris, H., & Pellet, F. (2019). Effect of the injection scenario on the rate and magnitude content of injection-induced seismicity: Case of a heterogeneous fault. *Journal of Geophysical Research: Solid*

Earth, *124*(8), 8426–8448. doi: 10.1029/2019JB017898

Ampuero, J.-P., & Rubin, A. M. (2008). Earthquake nucleation on rate and state faults–aging and slip laws. *Journal of Geophysical Research: Solid Earth*, *113*(B1). doi: 10.1029/2007JB005082

Andrés, S., Santillán, D., Mosquera, J. C., & Cueto-Felgueroso, L. (2019). Delayed weakening and reactivation of rate-and-state faults driven by pressure changes due to fluid injection. *Journal of Geophysical Research: Solid Earth*, *124*(11), 11917–11937. doi: 10.1029/2019JB018109

Bernab, Y., Mok, U., & Evans, B. (2003). Permeability-porosity relationships in rocks subjected to various evolution processes. *Pure & Applied Geophysics*, *160*(5-6), 937-960. doi: 10.1007/PL00012574

Bhattacharya, P., Rubin, A. M., & Beeler, N. M. (2017). Does fault strengthening in laboratory rock friction experiments really depend primarily upon time and not slip? *Journal of Geophysical Research: Solid Earth*, *122*(8), 6389–6430. doi: 10.1002/2017JB013936

Bhattacharya, P., & Viesca, R. C. (2019). Fluid-induced aseismic fault slip outpaces pore-fluid migration. *Science*, *364*(6439), 464–468. doi: 10.1126/science.aaw7354

Brantut, N. (2020). Dilatancy-induced fluid pressure drop during dynamic rupture: Direct experimental evidence and consequences for earthquake dynamics. *Earth and Planetary Science Letters*, *538*, 116179. doi: 10.1016/j.epsl.2020.116179

Cappa, F., Guglielmi, Y., Nussbaum, C., & Birkholzer, J. (2018). On the relationship between fault permeability increases, induced stress perturbation, and the growth of aseismic slip during fluid injection. *Geophysical Research Letters*, *45*(20), 11–012. doi: 10.1029/2018GL080233

Cappa, F., Scuderi, M. M., Collettini, C., Guglielmi, Y., & Avouac, J.-P. (2019). Stabilization of fault slip by fluid injection in the laboratory and in situ. *Science advances*, *5*(3), eaau4065. doi: 10.1126/sciadv.aau4065

Chang, K. W., & Segall, P. (2016). Injection-induced seismicity on basement faults including poroelastic stressing. *Journal of Geophysical Research: Solid Earth*, *121*(4), 2708–2726. doi: 10.1002/2015JB012561

Civan, F. (2001). Scale effect on porosity and permeability: Kinetics, model, and correlation. *AIChE journal*, *47*(2), 271–287. doi: 10.1002/aic.690470206

Cornet, F. H., Helm, J., Poitrenaud, H., & Etchecopar, A. (1997). Seismic and aseismic slips induced by large-scale fluid injections. In *Seismicity associated with mines, reservoirs and fluid injections* (pp. 563–583). doi: 10.1007/978-3-0348-8814-1_12

David, C., Wong, T. F., Zhu, W., & Zhang, J. (1994). Laboratory measurement of compaction-induced permeability change in porous rocks: Implications for the generation and maintenance of pore pressure excess in the crust. *Pure & Applied Geophysics*, *143*(1-3), 425-456. doi: 10.1007/BF00874337

De Barros, L., Cappa, F., Deschamps, A., & Dublanchet, P. (2020). Imbricated aseismic slip and fluid diffusion drive a seismic swarm in the Corinth Gulf, Greece. *Geophysical Research Letters*, *47*(9), e2020GL087142. doi: 10.1029/2020GL087142

Deng, K., Liu, Y., & Harrington, R. M. (2016). Poroelastic stress triggering of the December 2013 Crooked Lake, Alberta, induced seismicity sequence. *Geophysical Research Letters*, *43*(16), 8482–8491. doi: 10.1002/2016GL070421

Dieterich, J. H. (1992). Earthquake nucleation on faults with rate-and state-dependent strength. *Tectonophysics*, *211*(1-4), 115–134. doi: 10.1016/0040-1951(92)90055-B

Dieterich, J. H., Richards-Dinger, K. B., & Kroll, K. A. (2015). Modeling injection-induced seismicity with the physics-based earthquake simulator RSQSim. *Seismological Research Letters*, *86*(4), 1102–1109. doi: 10.1785/0220150057

Dublanchet, P. (2018, 10). Inferring fault slip rates from cumulative seismic moment in a multiple asperity context. *Geophysical Journal International*, *216*(1), 395-413. doi: 10.1093/gji/ggy431

Dublanchet, P. (2019). Fluid driven shear cracks on a strengthening rate-and-state frictional fault. *Journal of the Mechanics and Physics of Solids*, *132*, 103672. doi: 10.1016/j.jmps.2019.07.015

Dublanchet, P., Bernard, P., & Favreau, P. (2013). Interactions and triggering in a 3-d rate-and-state asperity model. *Journal of Geophysical Research: Solid Earth*, *118*(5), 2225–2245. doi: 10.1002/jgrb.50187

Duboeuf, L., De Barros, L., Cappa, F., Guglielmi, Y., Deschamps, A., & Seguy, S. (2017). Aseismic motions drive a sparse seismicity during fluid injections into a fractured zone in a carbonate reservoir. *Journal of Geophysical Research: Solid Earth*, *122*(10), 8285–8304. doi: 10.1002/2017JB014535

Duru, K., Allison, K. L., Rivet, M., & Dunham, E. M. (2019). Dynamic rupture and earthquake sequence simulations using the wave equation in second-order form. *Geophysical Journal International*, *219*(2), 796–815. doi: 10.1093/gji/ggz319

Duverger, C., Godano, M., Bernard, P., Lyon-Caen, H., & Lambotte, S. (2015). The 2003–2004 seismic swarm in the western corinth rift: Evidence for a multiscale pore pressure diffusion process along a permeable fault system. *Geophysical Research Letters*, *42*(18), 7374–7382. doi: 10.1002/2015GL065298

Ellsworth, W. L. (2013). Injection-induced earthquakes. *Science*, *341*(6142). doi: 10.1126/science.1225942

Elsworth, D., Spiers, C. J., & Niemeijer, A. R. (2016). Understanding induced seismicity. *Science*, *354*(6318), 1380–1381. doi: 10.1126/science.aal2584

Erickson, B. A., & Dunham, E. M. (2014). An efficient numerical method for earthquake cycles in heterogeneous media: Alternating subbasin and surface-rupturing events on faults crossing a sedimentary basin. *Journal of Geophysical Research: Solid Earth*, *119*(4), 3290–3316. doi: 10.1002/2013JB010614

Evans, K. F. (2001). Determining the effect of stimulation injections on the rock mass around the well gpk1 from borehole data: Analysis of the 1993 injections. *Data Analysis and Controls Towards Understanding Reservoir Behaviour and the Creating of a Conceptual Reservoir Models*, 6–74.

Evans, K. F., Moriya, H., Niitsuma, H., Jones, R. H., Phillips, W. S., Genter, A., ... Baria, R. (2005). Microseismicity and permeability enhancement of hydrogeologic structures during massive fluid injections into granite at 3 km depth at the Soultz HDR site. *Geophysical Journal International*, *160*(1), 388–412. doi: 10.1111/j.1365-246X.2004.02474.x

Eyre, T. S., Eaton, D. W., Garagash, D. I., Zecevic, M., Venieri, M., Weir, R., & Lawton, D. C. (2019). The role of aseismic slip in hydraulic fracturing–induced seismicity. *Science advances*, *5*(8), eaav7172. doi: 10.1126/sciadv.aav7172

Eyre, T. S., Zecevic, M., Salvage, R. O., & Eaton, D. W. (2020). A long-lived swarm of hydraulic fracturing-induced seismicity provides evidence for aseismic slip. *Bulletin of the Seismological Society of America*. doi: 10.1785/0120200107

Faulkner, D. R., & Rutter, E. H. (2001). Can the maintenance of overpressured fluids in large strike-slip fault zones explain their apparent weakness? *Geology*, *29*(6), 503–506. doi: 10.1130/0091-7613(2001)029⟨0503:CTMOOF⟩2.0.CO;2

Faulkner, D. R., Sanchez-Roa, C., Boulton, C., & Den Hartog, S. A. M. (2018). Pore fluid pressure development in compacting fault gouge in theory, experiments, and nature. *Journal of Geophysical Research: Solid Earth*, *123*(1), 226–241. doi: 10.1002/2017JB015130

French, M. E., Zhu, W., & Banker, J. (2016). Fault slip controlled by stress path and fluid pressurization rate. *Geophysical Research Letters*, *43*(9), 4330–4339. doi: 10.1002/2016GL068893

Garagash, D. I., & Germanovich, L. N. (2012). Nucleation and arrest of dynamic slip on a pressurized fault. *Journal of Geophysical Research: Solid Earth*,

117(B10). doi: 10.1029/2012JB009209

Goebel, T. H. W., & Brodsky, E. E. (2018). The spatial footprint of injection wells in a global compilation of induced earthquake sequences. *Science*, *361*(6405), 899–904. doi: 10.1126/science.aat5449

Goebel, T. H. W., Hosseini, S. M., Cappa, F., Hauksson, E., Ampuero, J. P., Aminzadeh, F., & Saleeby, J. B. (2016). Wastewater disposal and earthquake swarm activity at the southern end of the Central Valley, California. *Geophysical Research Letters*, *43*(3), 1092–1099. doi: 10.1002/2015GL066948

Goebel, T. H. W., Weingarten, M., Chen, X., Haffener, J., & Brodsky, E. E. (2017). The 2016 Mw 5.1 Fairview, Oklahoma earthquakes: Evidence for long-range poroelastic triggering at ¿40 km from fluid disposal wells. *Earth and Planetary Science Letters*, *472*, 50–61. doi: 10.1016/j.epsl.2017.05.011

Guglielmi, Y., Cappa, F., Avouac, J.-P., Henry, P., & Elsworth, D. (2015). Seismicity triggered by fluid injection–induced aseismic slip. *Science*, *348*(6240), 1224–1226. doi: 10.1126/science.aab0476

Handin, J. (1969). On the Coulomb-Mohr failure criterion. *Journal of Geophysical Research*, *74*(22), 5343–5348. doi: 10.1029/JB074i022p05343

Häring, M. O., Schanz, U., Ladner, F., & Dyer, B. C. (2008). Characterisation of the basel 1 enhanced geothermal system. *Geothermics*, *37*(5), 469–495. doi: 10.1016/j.geothermics.2008.06.002

Heimisson, E. R., Dunham, E. M., & Almquist, M. (2019). Poroelastic effects destabilize mildly rate-strengthening friction to generate stable slow slip pulses. *Journal of the Mechanics and Physics of Solids*, *130*, 262–279. doi: 10.1016/j.jmps.2019.06.007

Hirakawa, E., & Ma, S. (2016). Dynamic fault weakening and strengthening by gouge compaction and dilatancy in a fluid-saturated fault zone. *Journal of Geophysical Research: Solid Earth*, *121*(8), 5988–6008. doi: 10.1002/2015JB012509

Horton, S. (2012). Disposal of hydrofracking waste fluid by injection into subsurface aquifers triggers earthquake swarm in central Arkansas with potential for damaging earthquake. *Seismological Research Letters*, *83*(2), 250–260. doi: 10.1785/gssrl.83.2.250

Im, K., Elsworth, D., & Fang, Y. (2018). The influence of preslip sealing on the permeability evolution of fractures and faults. *Geophysical Research Letters*, *45*(1), 166–175. doi: 10.1002/2017GL076216

Im, K., Elsworth, D., & Wang, C. (2019). Cyclic permeability evolution during repose then reactivation of fractures and faults. *Journal of Geophysical Research: Solid Earth*, *124*(5), 4492–4506. doi: 10.1029/2019JB017309

Jiang, J., & Lapusta, N. (2016). Deeper penetration of large earthquakes on seismically quiescent faults. *Science*, *352*(6291), 1293–1297. doi: 10.1126/science.aaf1496

Jiang, J., & Lapusta, N. (2017). Connecting depth limits of interseismic locking, microseismicity, and large earthquakes in models of long-term fault slip. *Journal of Geophysical Research: Solid Earth*, *122*(8), 6491–6523. doi: 10.1002/2017JB014030

Johannes, H., Coltman, E., & Class, H. (2018). Porositypermeability relations for evolving pore space: A review with a focus on (bio-)geochemically altered porous media. *Transport in Porous Media*, *124*, 589-629. doi: 10.1007/s11242-018-1086-2

Keranen, K. M., Savage, H. M., Abers, G. A., & Cochran, E. S. (2013). Potentially induced earthquakes in Oklahoma, USA: Links between wastewater injection and the 2011 Mw 5.7 earthquake sequence. *Geology*, *41*(6), 699–702. doi: 10.1126/science.1255802

Kim, K. H., Ree, J. H., Kim, Y. H., Kim, S. S., Kang, S. Y., & Seo, W. S. (2018). Assessing whether the 2017 Mw 5.4 Pohang earthquake in South Korea was an

induced event. *Science*, *360*(6392), 1007–1009. doi: 10.1126/science.aat6081

Kim, W. Y. (2013). Induced seismicity associated with fluid injection into a deep well in Youngstown, Ohio. *Journal of Geophysical Research: Solid Earth*, *118*(7), 3506–3518. doi: 10.1002/jgrb.50247

Kohli, A. H., & Zoback, M. D. (2013). Frictional properties of shale reservoir rocks. *Journal of geophysical research: solid earth*, *118*(9), 5109–5125. doi: 10.1002/jgrb.50346

Kozdon, J. E., Dunham, E. M., & Nordström, J. (2013). Simulation of dynamic earthquake ruptures in complex geometries using high-order finite difference methods. *Journal of Scientific Computing*, *55*(1), 92–124. doi: 10.1007/s10915-012-9624-5

Larochelle, S., Lapusta, N., Ampuero, J.-P., & Cappa, F. (2020). *Constraining fault friction and stability with fluid injection field experiments.* (https://www.essoar.org/doi/abs/10.1002/essoar.10504514.1)

Lengliné, O., Boubacar, M., & Schmittbuhl, J. (2017). Seismicity related to the hydraulic stimulation of grt1, rittershoffen, france. *Geophysical Journal International*, *208*(3), 1704–1715. doi: 10.1093/gji/ggw490

Lockner, D. A., & Byerlee, J. D. (1994). Dilatancy in hydraulically isolated faults and the suppression of instability. *Geophysical Research Letters*, *21*(22), 2353–2356. doi: 10.1029/94GL02366

Lui, S. K. Y., & Lapusta, N. (2016). Repeating microearthquake sequences interact predominantly through postseismic slip. *Nature communications*, *7*(1), 1–7. doi: 10.1038/ncomms13020

Luo, Y., & Ampuero, J.-P. (2018). Stability of faults with heterogeneous friction properties and effective normal stress. *Tectonophysics*, *733*, 257–272. doi: 10.1016/j.tecto.2017.11.006

Luquot, L., & Gouze, P. (2009). Experimental determination of porosity and permeability changes induced by injection of CO2 into carbonate rocks. *Chemical Geology*, *265*(1-2), 148–159. doi: 10.1016/j.chemgeo.2009.03.028

Mase, C. W., & Smith, L. (1987). Effects of frictional heating on the thermal, hydrologic, and mechanical response of a fault. *Journal of Geophysical Research: Solid Earth*, *92*(B7), 6249–6272. doi: 10.1029/JB092iB07p06249

Mazzoldi, A., Rinaldi, A. P., Borgia, A., & Rutqvist, J. (2012). Induced seismicity within geological carbon sequestration projects: maximum earthquake magnitude and leakage potential from undetected faults. *International Journal of Greenhouse Gas Control*, *10*, 434–442. doi: 10.1016/j.ijggc.2012.07.012

McClure, M. W., & Horne, R. N. (2011). Investigation of injection-induced seismicity using a coupled fluid flow and rate/state friction model. *Geophysics*, *76*(6), WC181–WC198. doi: 10.1190/GEO2011-0064.1

McGarr, A., Bekins, B., Burkardt, N., Dewey, J., Earle, P., Ellsworth, W., ... Majer, E. (2015). Coping with earthquakes induced by fluid injection. *Science*, *347*(6224), 830–831. doi: 10.1126/science.aaa0494

Menke, H. P., Bijeljic, B., Andrew, M. G., & Blunt, M. J. (2015). Dynamic three-dimensional pore-scale imaging of reaction in a carbonate at reservoir conditions. *Environmental science & technology*, *49*(7), 4407–4414. doi: 10.1021/es505789f

Morrow, C. A., & Byerlee, J. D. (1989). Experimental studies of compaction and dilatancy during frictional sliding on faults containing gouge. *J. Struct. Geol*, *11*(7), 815–825. doi: 10.1016/0191-8141(89)90100-4

Nelson, P. H. (1994). Permeability-porosity relationships in sedimentary rocks. *The Log Analyst*, *35*(03).

Norbeck, J. H., & Horne, R. N. (2018). Maximum magnitude of injection-induced earthquakes: A criterion to assess the influence of pressure migration along faults. *Tectonophysics*, *733*, 108–118. doi: 10.1016/j.tecto.2018.01.028

Pampillón, P., Santillán, D., Mosquera, J. C., & Cueto-Felgueroso, L. (2018). Dy-

namic and quasi-dynamic modeling of injection-induced earthquakes in poroelastic media. *Journal of Geophysical Research: Solid Earth*, *123*(7), 5730–5759. doi: 10.1029/2018JB015533

Proctor, B., Lockner, D. A., Kilgore, B. D., Mitchell, T. M., & Beeler, N. M. (2020). Direct evidence for fluid pressure, dilatancy, and compaction affecting slip in isolated faults. *Geophysical Research Letters*, e2019GL086767. doi: 10.1029/2019GL086767

Rawling, G. C., Baud, P., & Wong, T. F. (2002). Dilatancy, brittle strength, and anisotropy of foliated rocks: Experimental deformation and micromechanical modeling. *Journal of Geophysical Research: Solid Earth*, *107*(B10), ETG–8. doi: 10.1029/2001JB000472

Rice, J. R. (1992). Fault stress states, pore pressure distributions, and the weakness of the san andreas fault. In *International geophysics* (Vol. 51, pp. 475–503). Elsevier.

Rice, J. R. (1993). Spatio-temporal complexity of slip on a fault. *Journal of Geophysical Research: Solid Earth*, *98*(B6), 9885–9907. doi: 10.1029/93JB00191

Rice, J. R. (2006). Heating and weakening of faults during earthquake slip. *Journal of Geophysical Research: Solid Earth*, *111*(B5). doi: 10.1029/2005JB004006

Rice, J. R., Lapusta, N., & Ranjith, K. (2001). Rate and state dependent friction and the stability of sliding between elastically deformable solids. *Journal of the Mechanics and Physics of Solids*, *49*(9), 1865–1898. doi: 10.1016/S0022-5096(01)00042-4

Roland, E., & McGuire, J. J. (2009). Earthquake swarms on transform faults. *Geophysical Journal International*, *178*(3), 1677–1690. doi: 10.1111/j.1365-246X.2009.04214.x

Ross, Z. E., Cochran, E. S., Trugman, D. T., & Smith, J. D. (2020). 3d fault architecture controls the dynamism of earthquake swarms. *Science*, *368*(6497), 1357–1361. doi: 10.1126/science.abb0779

Ruina, A. (1983). Slip instability and state variable friction laws. *Journal of Geophysical Research: Solid Earth*, *88*(B12), 10359–10370. doi: 10.1029/JB088iB12p10359

Saffer, D. M., & Tobin, H. J. (2011). Hydrogeology and mechanics of subduction zone forearcs: Fluid flow and pore pressure. *Annual Review of Earth and Planetary Sciences*, *39*, 157–186. doi: 10.1146/annurev-earth-040610-133408

Samuelson, J., Elsworth, D., & Marone, C. (2009). Shear-induced dilatancy of fluid-saturated faults: Experiment and theory. *Journal of Geophysical Research: Solid Earth*, *114*(B12). doi: 10.1029/2008JB006273

Savage, H. M., Kirkpatrick, J. D., Mori, J. J., Brodsky, E. E., Ellsworth, W. L., Carpenter, B. M., ... Kano, Y. (2017). Scientific exploration of induced seismicity and stress (SEISMS). *Scientific Drilling*, *23*. doi: 10.5194/sd-23-57-2017

Scuderi, M. M., Collettini, C., & Marone, C. (2017). Frictional stability and earthquake triggering during fluid pressure stimulation of an experimental fault. *Earth and Planetary Science Letters*, *477*, 84–96. doi: 10.1016/j.epsl.2017.08.009

Segall, P., & Lu, S. (2015). Injection-induced seismicity: Poroelastic and earthquake nucleation effects. *Journal of Geophysical Research: Solid Earth*, *120*(7), 5082–5103. doi: 10.1002/2015JB012060

Segall, P., & Rice, J. R. (1995). Dilatancy, compaction, and slip instability of a fluid-infiltrated fault. *Journal of Geophysical Research: Solid Earth*, *100*(B11), 22155–22171. doi: 10.1029/95JB02403

Segall, P., Rubin, A. M., Bradley, A. M., & Rice, J. R. (2010). Dilatant strengthening as a mechanism for slow slip events. *Journal of Geophysical Research: Solid Earth*, *115*(B12). doi: 10.1029/2010JB007449

Shapiro, S. A., & Dinske, C. (2009). Scaling of seismicity induced by nonlinear fluid-rock interaction. *Journal of Geophysical Research: Solid Earth*, *114*(B9). doi:

10.1029/2008JB006145

Shapiro, S. A., Huenges, E., & Borm, G. (1997). Estimating the crust permeability from fluid-injection-induced seismic emission at the KTB site. *Geophysical Journal International*, *131*(2), F15–F18. doi: 10.1111/j.1365-246X.1997.tb01215.x

Shelly, D. R., Ellsworth, W. L., & Hill, D. P. (2016). Fluid-faulting evolution in high definition: Connecting fault structure and frequency-magnitude variations during the 2014 Long Valley Caldera, California, earthquake swarm. *Journal of Geophysical Research: Solid Earth*, *121*(3), 1776–1795. doi: 10.1002/2015JB012719

Shelly, D. R., Hill, D. P., Massin, F., Farrell, J., Smith, R. B., & Taira, T. (2013). A fluid-driven earthquake swarm on the margin of the Yellowstone caldera. *Journal of Geophysical Research: Solid Earth*, *118*(9), 4872–4886. doi: doi:10.1002/jgrb.50362

Simpson, G., Guéguen, Y., & Schneider, F. (2001). Permeability enhancement due to microcrack dilatancy in the damage regime. *Journal of Geophysical Research: Solid Earth*, *106*(B3), 3999–4016. doi: 10.1029/2000JB900194

Szafranski, D., & Duan, B. (2020, 08). Exploring Physical Links between Fluid Injection and Nearby Earthquakes: The 2012 Mw 4.8 Timpson, Texas, Case Study. *Bulletin of the Seismological Society of America*. doi: 10.1785/0120200090

Tanikawa, W., Mukoyoshi, H., Tadai, O., Hirose, T., Tsutsumi, A., & Lin, W. (2012). Velocity dependence of shear-induced permeability associated with frictional behavior in fault zones of the Nankai subduction zone. *Journal of Geophysical Research: Solid Earth*, *117*(B5). doi: 10.1029/2011JB008956,

Torberntsson, K., Stiernström, V., Mattsson, K., & Dunham, E. M. (2018). A finite difference method for earthquake sequences in poroelastic solids. *Computational Geosciences*, *22*(5), 1351–1370. doi: 10.1007/s10596-018-9757-1

Viesca, R. C. (2020). *On the existence of a nucleation length for dynamic shear rupture.* (arXiv:submit/3340971)

Villiger, L., Gischig, S., Doetsch, J., Krietsch, H., Dutler, O., Jalali, M., ... others (2020). Influence of reservoir geology on seismic response during decameter-scale hydraulic stimulations in crystalline rock. *Solid Earth*, *11*(2), 627–655. doi: 10.5194/se-11-627-2020

Walder, J., & Nur, A. (1984). Porosity reduction and crustal pore pressure development. *Journal of Geophysical Research: Solid Earth*, *89*(B13), 11539–11548. doi: 10.1029/JB089iB13p11539

Wang, H. F. (2017). *Theory of linear poroelasticity with applications to geomechanics and hydrogeology.* Princeton: Princeton University Press.

Wang, L., Kwiatek, G., Rybacki, E., Bonnelye, A., Bohnhoff, M., & Dresen, G. (2020). Laboratory study on fluid-induced fault slip behavior: The role of fluid pressurization rate. *Geophysical Research Letters*, *47*(6), e2019GL086627. doi: 10.1029/2019GL086627

Wei, S., Avouac, J.-P., Hudnut, K. W., Donnellan, A., Parker, J. W., Graves, R. W., ... Cappa, F. (2015). The 2012 Brawley swarm triggered by injection-induced aseismic slip. *Earth and Planetary Science Letters*, *422*, 115–125. doi: 10.1016/j.epsl.2015.03.054

Weingarten, M., Ge, S., Godt, J. W., Bekins, B. A., & Rubinstein, J. L. (2015). High-rate injection is associated with the increase in US mid-continent seismicity. *Science*, *348*(6241), 1336–1340. doi: 10.1126/science.aab1345

Wibberley, C. A. J. (2002). Hydraulic diffusivity of fault gouge zones and implications for thermal pressurization during seismic slip. *Earth, planets and space*, *54*(11), 1153–1171. doi: 10.1186/BF03353317

Wiprut, D., & Zoback, M. D. (2000). Fault reactivation and fluid flow along a previously dormant normal fault in the northern north sea. *Geology*, *28*(7), 595–

598. doi: 10.1130/0091-7613(2000)28⟨595:FRAFFA⟩2.0.CO;2

Wong, T. F., David, C., & Zhu, W. (1997). The transition from brittle faulting to cataclastic flow in porous sandstones: Mechanical deformation. *Journal of Geophysical Research: Solid Earth*, *102*(B2), 3009–3025. doi: 10.1029/96JB03281

Wynants-Morel, N., Cappa, F., De Barros, L., & Ampuero, J.-P. (2020). Stress perturbation from aseismic slip drives the seismic front during fluid injection in a permeable fault. *Journal of Geophysical Research: Solid Earth*, *125*, e2019JB019179. doi: 10.1029/2019JB019179

Yamashita, T. (2013). Generation of slow slip coupled with tremor due to fluid flow along a fault. *Geophysical Journal International*, *193*(1), 375–393. doi: 10.1093/gji/ggs117

Ye, Z., & Ghassemi, A. (2018). Injection-induced shear slip and permeability enhancement in granite fractures. *Journal of Geophysical Research: Solid Earth*, *123*(10), 9009–9032. doi: 10.1029/2018JB016045

Yeck, W. L., Hayes, G. P., McNamara, D. E., Rubinstein, J. L., Barnhart, W. D., Earle, P. S., & Benz, H. M. (2017). Oklahoma experiences largest earthquake during ongoing regional wastewater injection hazard mitigation efforts. *Geophysical Research Letters*, *44*(2), 711–717. doi: 10.1002/2016GL071685

Yehya, A., Yang, Z., & Rice, J. R. (2018). Effect of fault architecture and permeability evolution on response to fluid injection. *Journal of Geophysical Research: Solid Earth*, *123*(11), 9982–9997. doi: 10.1029/2018JB016550

Zhang, L., Soong, Y., Dilmore, R., & Lopano, C. (2015). Numerical simulation of porosity and permeability evolution of Mount Simon sandstone under geological carbon sequestration conditions. *Chemical Geology*, *403*, 1–12. doi: 10.1016/j.chemgeo.2015.03.014

Zhang, Y., Person, M., Rupp, J., Ellett, K., Celia, M. A., Gable, C. W., ... Mozley, P. (2013). Hydrogeologic controls on induced seismicity in crystalline basement rocks due to fluid injection into basal reservoirs. *Groundwater*, *51*(4), 525–538. doi: 10.1111/gwat.12071

Zhang, Y., Schaubs, P. M., Zhao, C., Ord, A., Hobbs, B. E., & Barnicoat, A. C. (2008). Fault-related dilation, permeability enhancement, fluid flow and mineral precipitation patterns: numerical models. *Geological Society, London, Special Publications*, *299*(1), 239–255. doi: 10.1144/SP299.15

Zhu, W., Allison, K. L., Dunham, E. M., & Yang, Y. (2020). Fault valving and pore pressure evolution in simulations of earthquake sequences and aseismic slip. *Nature Communications*, *11*(4833). doi: 10.1038/s41467-020-18598-z

Zhu, W., David, C., & Wong, T. F. (1995). Network modeling of permeability evolution during cementation and hot isostatic pressing. *Journal of Geophysical Research: Solid Earth*, *100*(B8), 15451–15464. doi: 10.1029/95JB00958

Zhu, W., & Wong, T. F. (1999). Network modeling of the evolution of permeability and dilatancy in compact rock. *Journal of Geophysical Research: Solid Earth*, *104*(B2), 2963–2971. doi: 10.1029/1998JB900062

Zoback, M. D., Kohli, A., Das, I., & McClure, M. W. (2012). The importance of slow slip on faults during hydraulic fracturing stimulation of shale gas reservoirs. In *SPE Americas Unconventional Resources Conference.*

Figure 1.

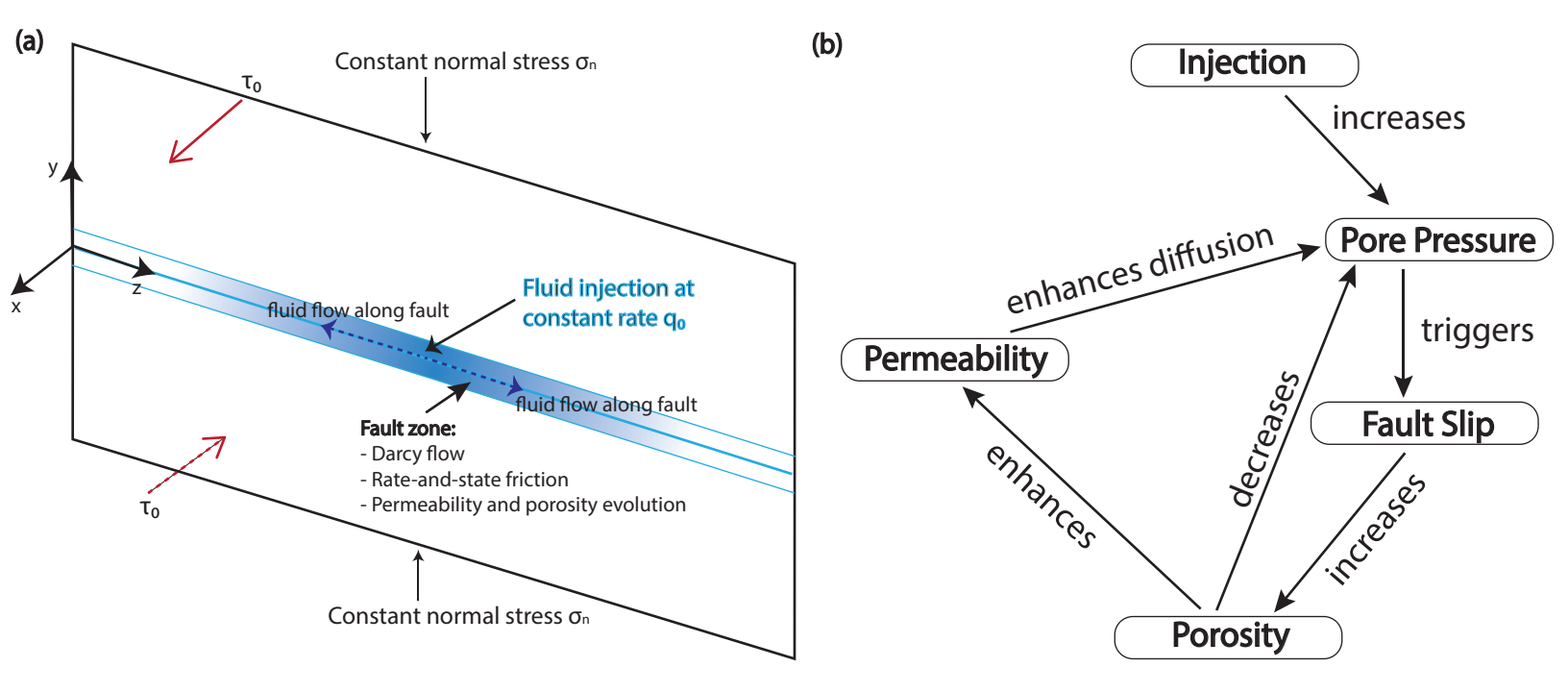
(a)
Constant normal stress σn
τ0
y
x
z
fluid flow along fault
Fluid injection at
constant rate q0
fluid flow along fault
Fault zone:
- Darcy flow
- Rate-and-state friction
- Permeability and porosity evolution
τ0
Constant normal stress σn
(b)
Injection
increases
Pore Pressure
enhances diffusion
Permeability
triggers
Fault Slip
enhances
decreases
increases
Porosity

Figure 2.

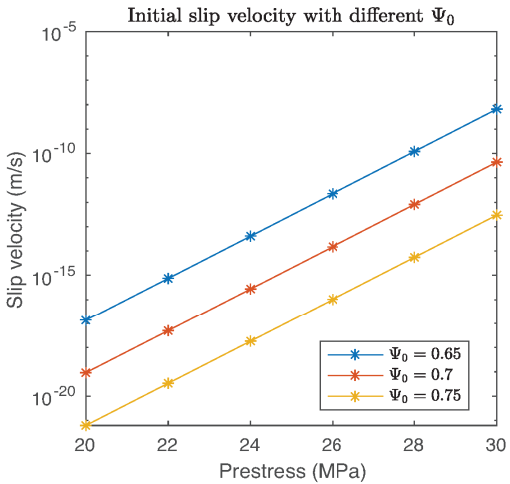
Initial slip velocity with different Ψ_0
Slip velocity (m/s)
Prestress (MPa)
$\Psi_0 = 0.65$
$\Psi_0 = 0.7$
$\Psi_0 = 0.75$

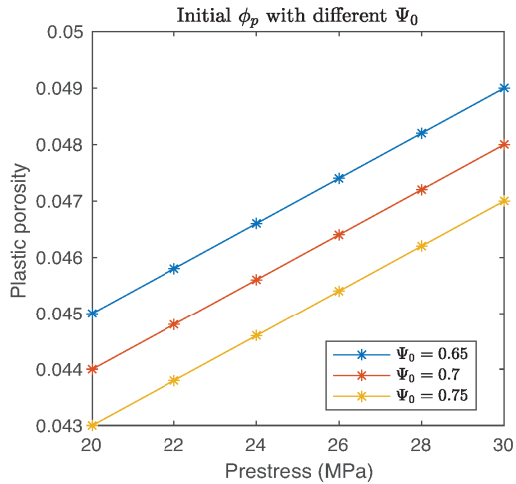
Initial ϕ_p with different Ψ_0
Plastic porosity
Prestress (MPa)
$\Psi_0 = 0.65$
$\Psi_0 = 0.7$
$\Psi_0 = 0.75$

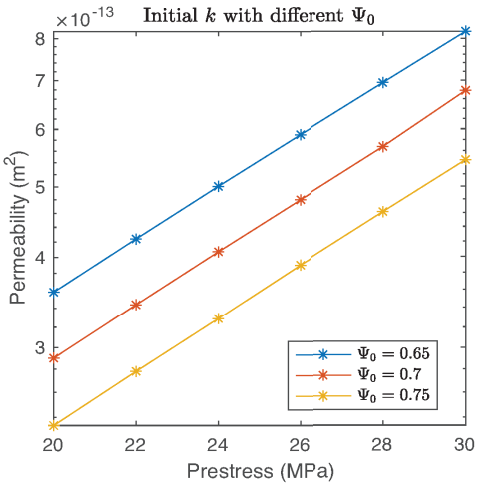
Initial k with different Ψ_0
Permeability (m^2)
Prestress (MPa)
$\Psi_0 = 0.65$
$\Psi_0 = 0.7$
$\Psi_0 = 0.75$

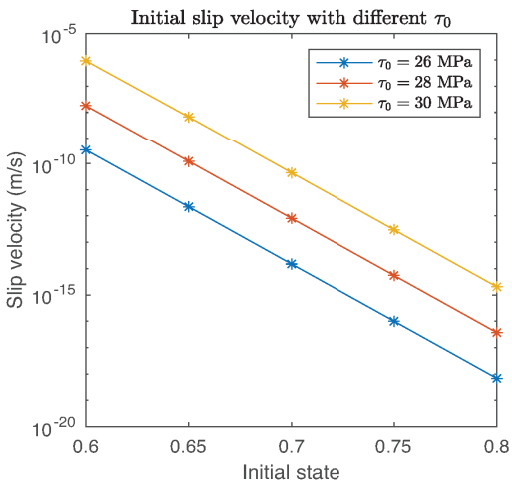
Initial slip velocity with different τ_0
Slip velocity (m/s)
Initial state
$\tau_0 = 26$ MPa
$\tau_0 = 28$ MPa
$\tau_0 = 30$ MPa

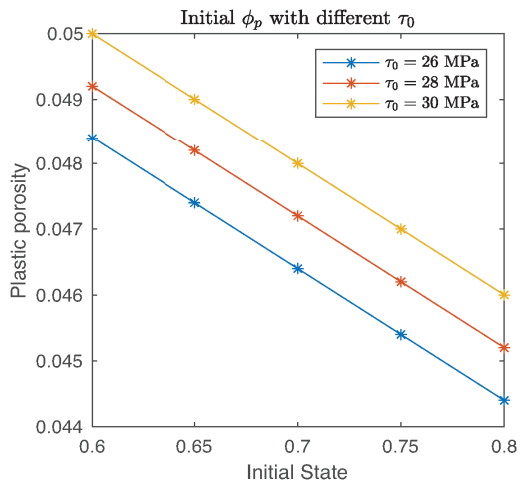
Initial ϕ_p with different τ_0
Plastic porosity
Initial State
$\tau_0 = 26$ MPa
$\tau_0 = 28$ MPa
$\tau_0 = 30$ MPa

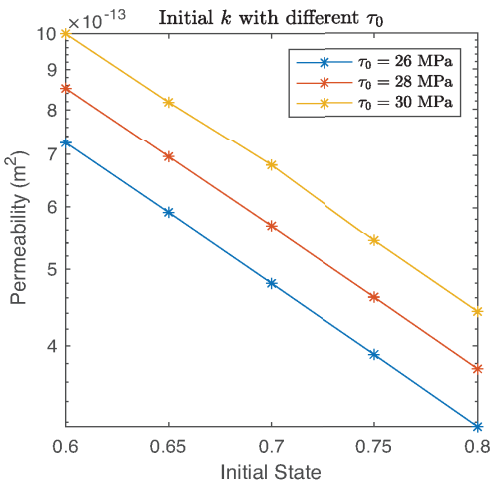
Initial k with different τ_0
Permeability (m^2)
Initial State
$\tau_0 = 26$ MPa
$\tau_0 = 28$ MPa
$\tau_0 = 30$ MPa

Figure 3.

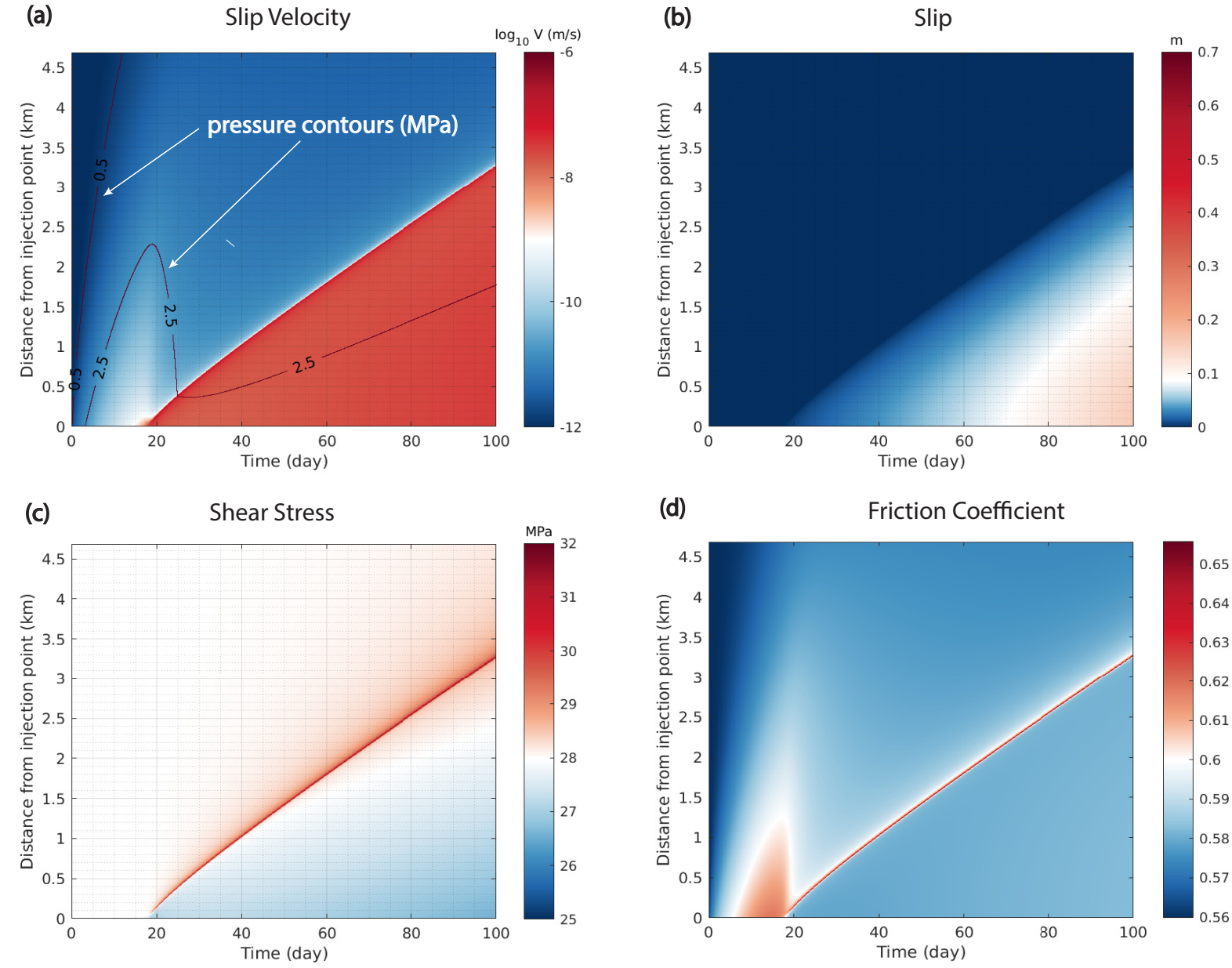
(a)
Slip Velocity
log10 V (m/s)
-6
-8
-10
-12
pressure contours (MPa)
0.5
2.5
2.5
2.5
0.5
Distance from injection point (km)
Time (day)
(b)
Slip
m
0.7
0.6
0.5
0.4
0.3
0.2
0.1
0
Distance from injection point (km)
Time (day)
(c)
Shear Stress
MPa
32
31
30
29
28
27
26
25
Distance from injection point (km)
Time (day)
(d)
Friction Coefficient
0.65
0.64
0.63
0.62
0.61
0.6
0.59
0.58
0.57
0.56
Distance from injection point (km)
Time (day)

Figure 4.

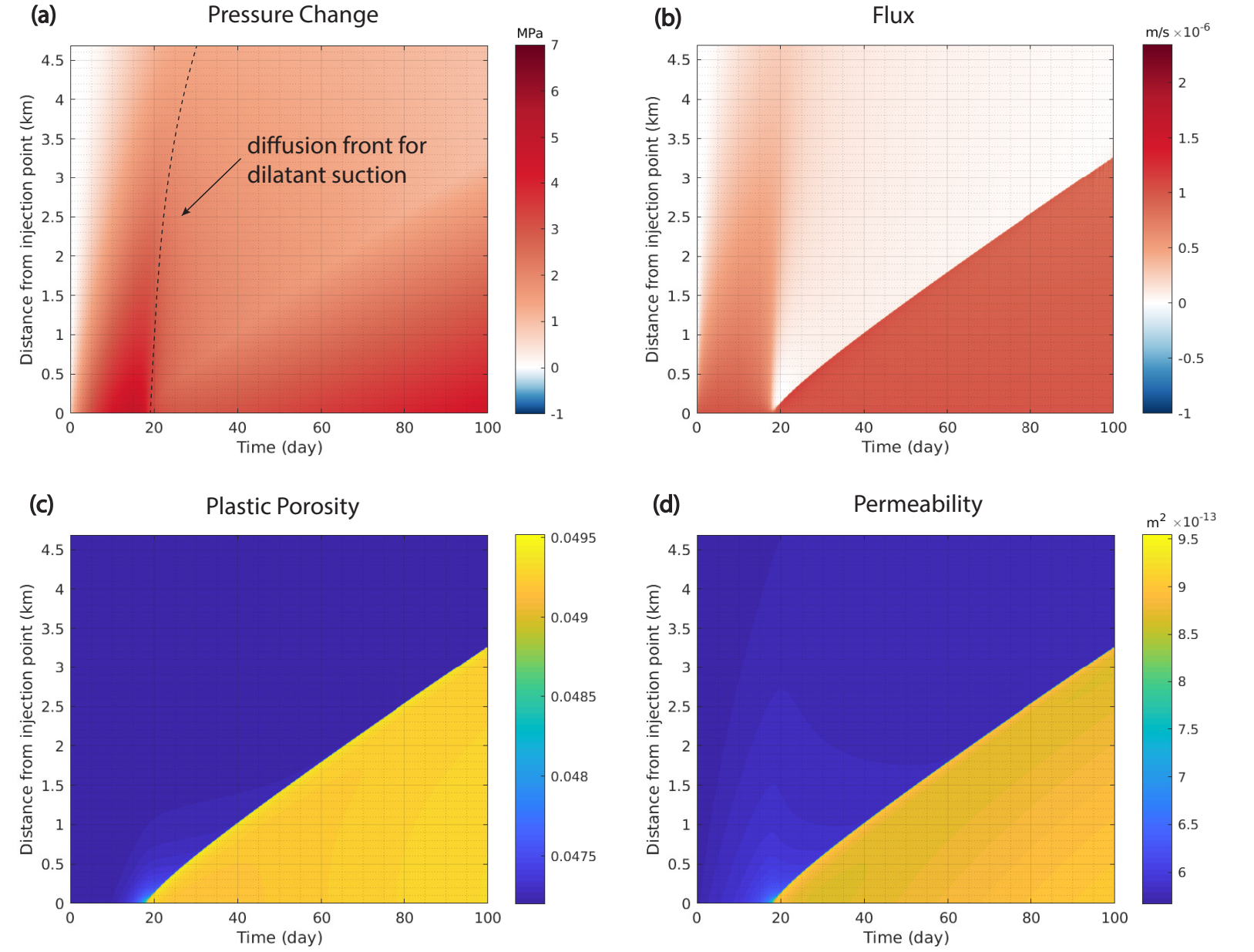
(a)
Pressure Change
MPa
diffusion front for
dilatant suction
Distance from injection point (km)
Time (day)
(b)
Flux
m/s ×10^-6
Distance from injection point (km)
Time (day)
(c)
Plastic Porosity
Distance from injection point (km)
Time (day)
(d)
Permeability
m^2 ×10^-13
Distance from injection point (km)
Time (day)

Figure 5.

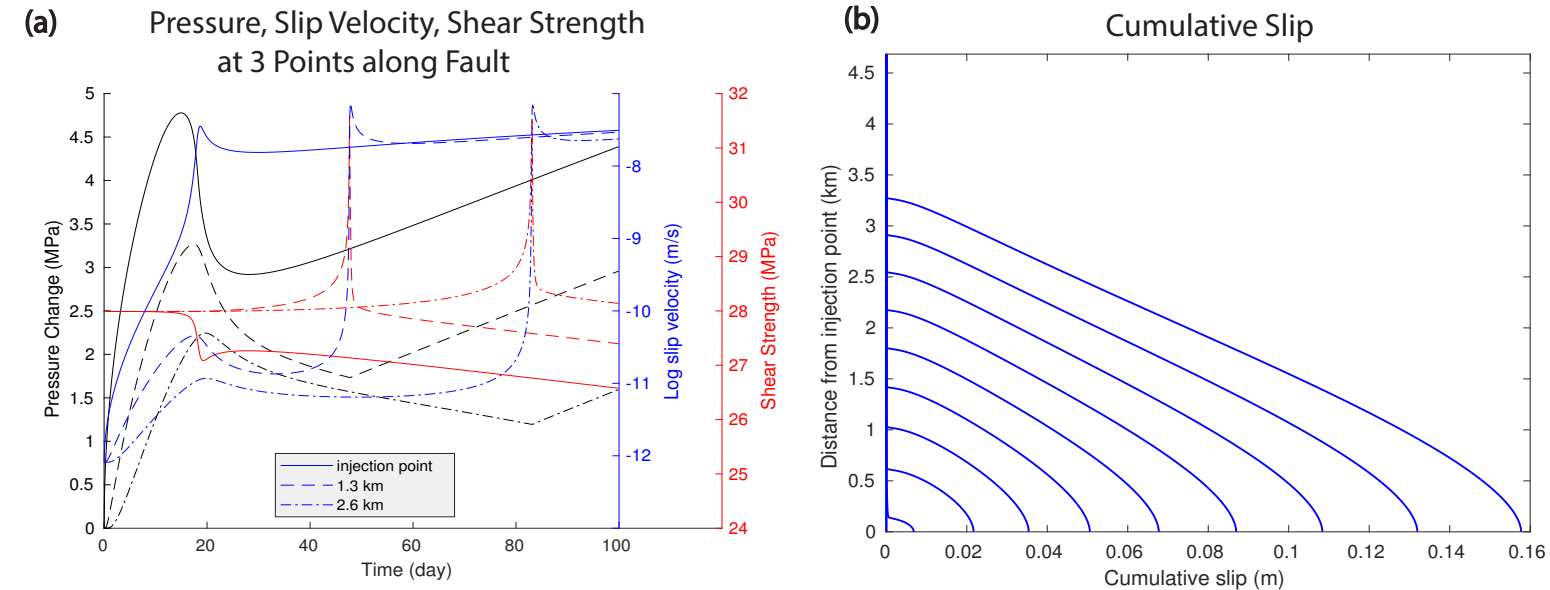
(a)
Pressure, Slip Velocity, Shear Strength at 3 Points along Fault
Pressure Change (MPa)
Log slip velocity (m/s)
Shear Strength (MPa)
Time (day)
injection point
1.3 km
2.6 km
(b)
Cumulative Slip
Distance from injection point (km)
Cumulative slip (m)

Figure 6.

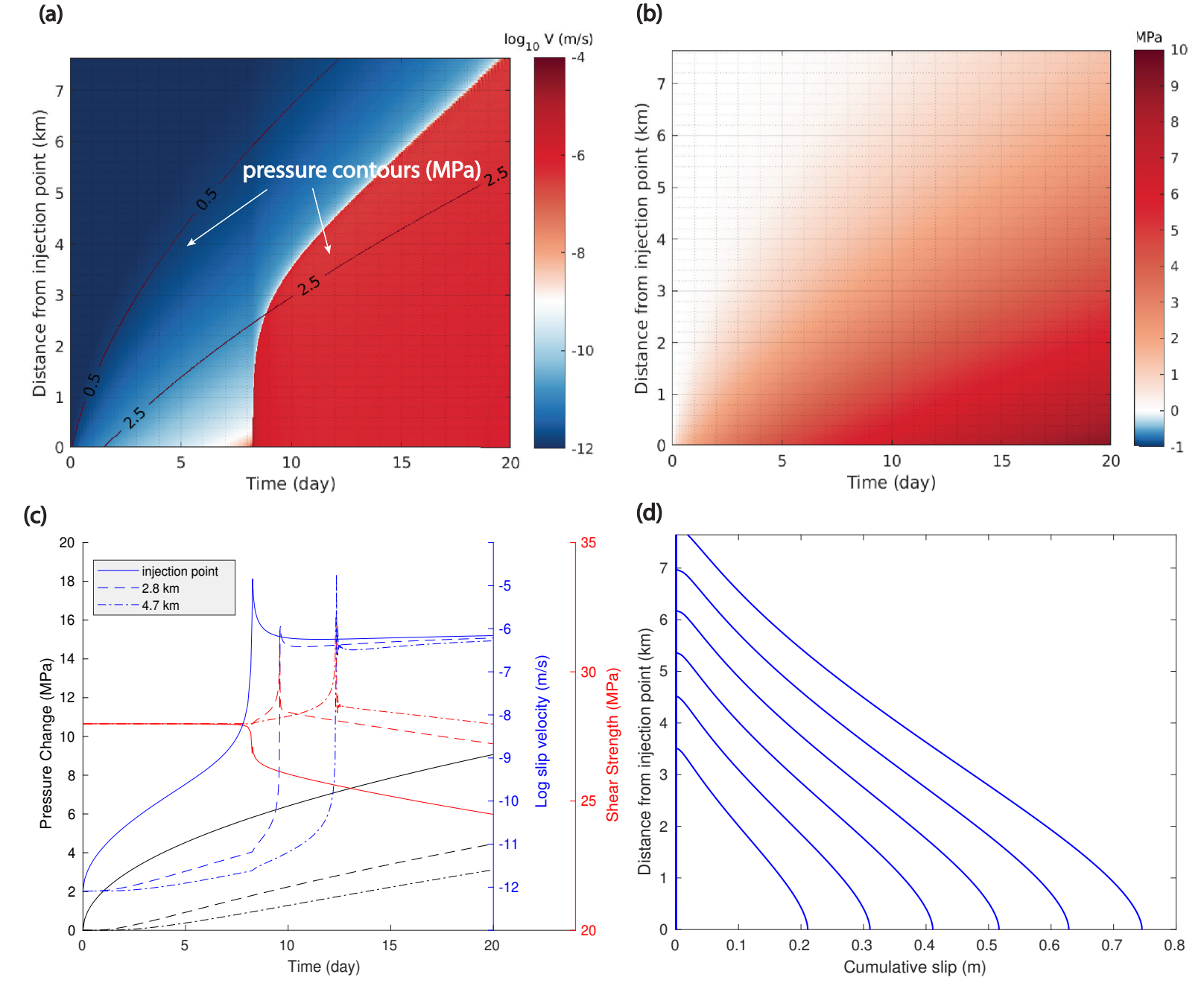
(a)
log10 V (m/s)
pressure contours (MPa)
0.5
2.5
2.5
0.5
2.5
Distance from injection point (km)
Time (day)
(b)
MPa
Distance from injection point (km)
Time (day)
(c)
injection point
2.8 km
4.7 km
Pressure Change (MPa)
Log slip velocity (m/s)
Shear Strength (MPa)
Time (day)
(d)
Distance from injection point (km)
Cumulative slip (m)

Figure 7.

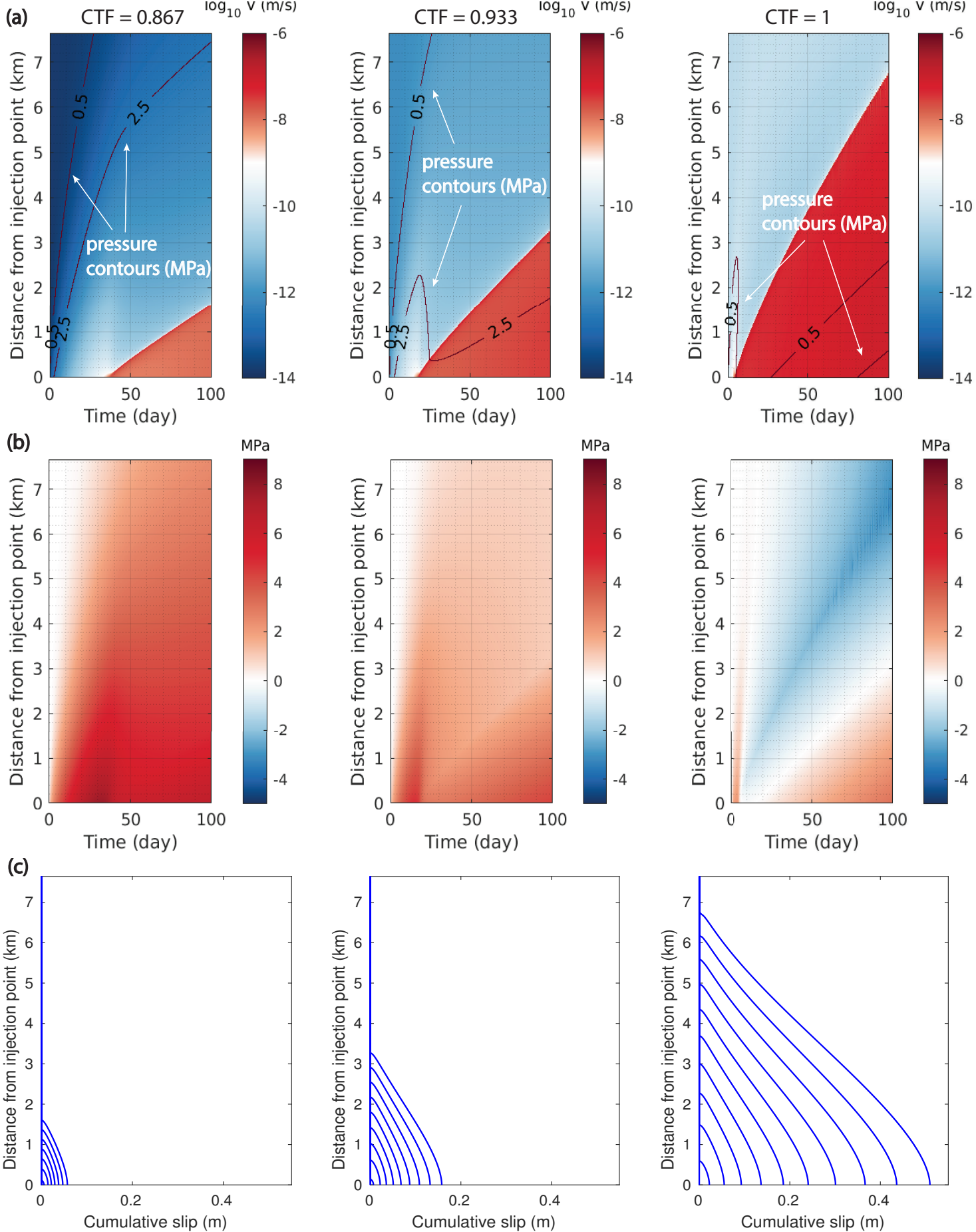
(a)
CTF = 0.867
CTF = 0.933
CTF = 1
log10 V (m/s)
pressure contours (MPa)
0.5
2.5
Distance from injection point (km)
Time (day)
(b)
MPa
(c)
Cumulative slip (m)

Figure 8.

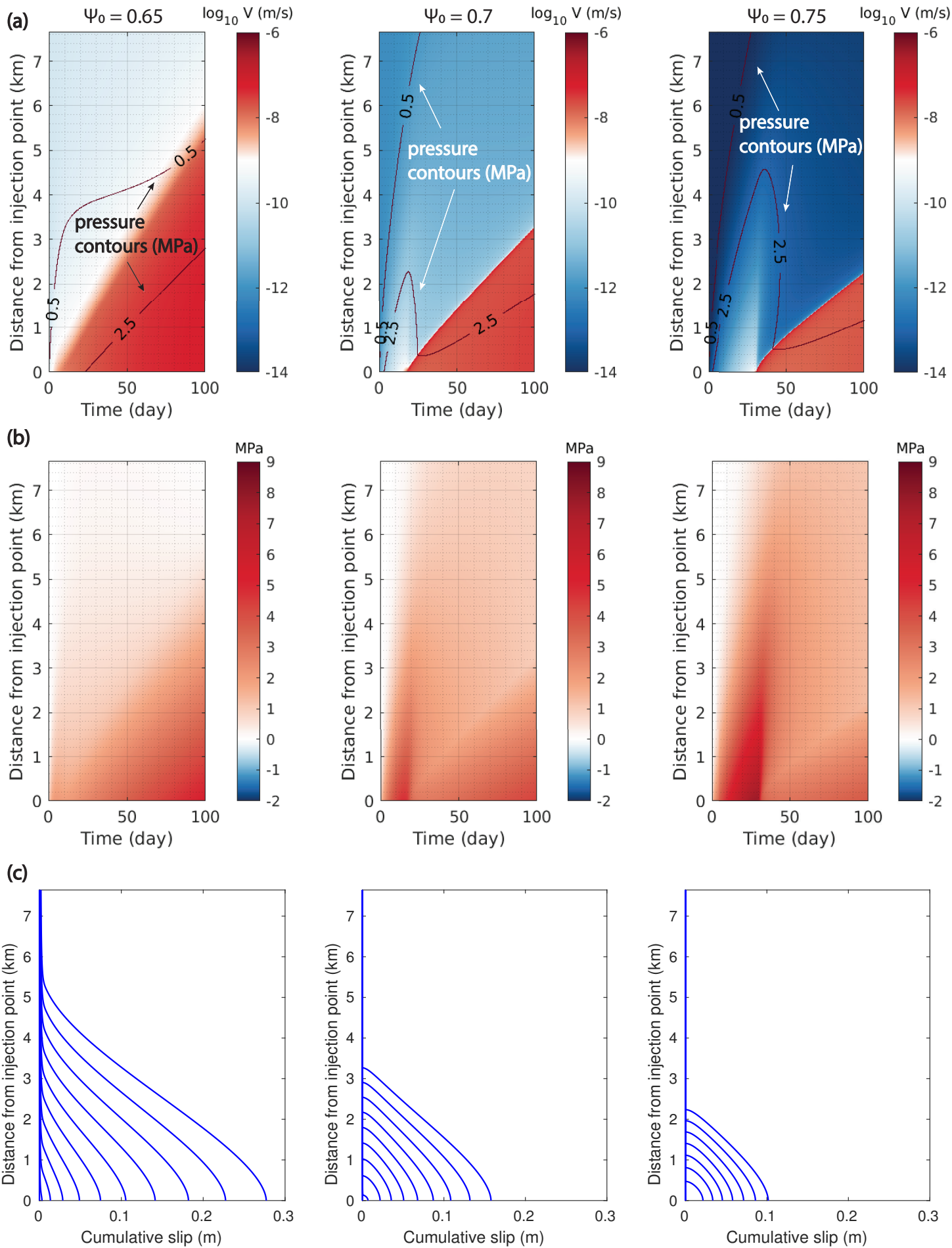
(a)
Ψ₀ = 0.65
Ψ₀ = 0.7
Ψ₀ = 0.75
log10 V (m/s)
-6
-8
-10
-12
-14
Distance from injection point (km)
Time (day)
pressure contours (MPa)
0.5
2.5
(b)
MPa
9
8
7
6
5
4
3
2
1
0
-1
-2
(c)
Cumulative slip (m)
0
0.1
0.2
0.3

Figure 9.

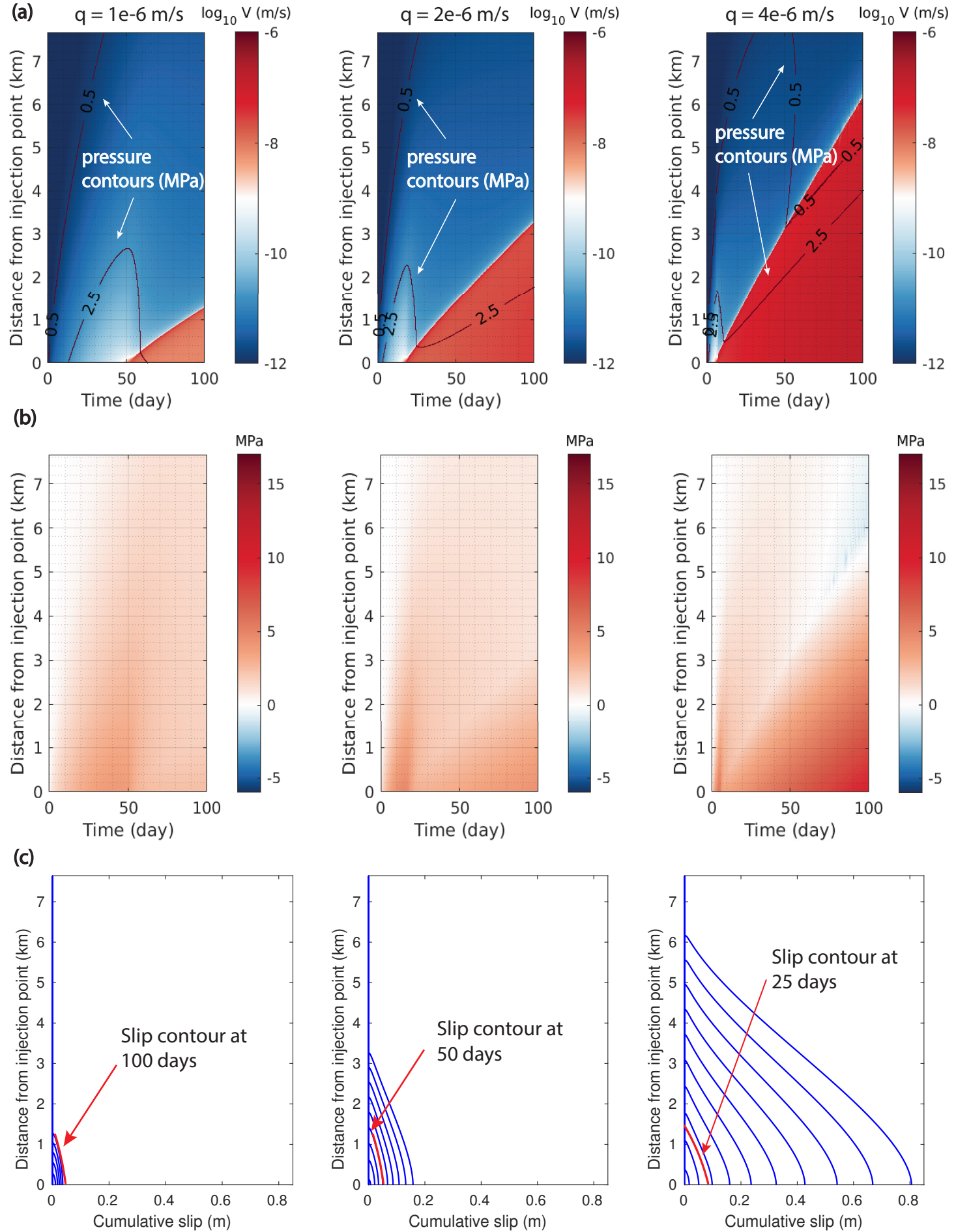
(a)
q = 1e-6 m/s
q = 2e-6 m/s
q = 4e-6 m/s
log10 V (m/s)
-6
-8
-10
-12
pressure contours (MPa)
0.5
2.5
Distance from injection point (km)
Time (day)
0
50
100
(b)
MPa
15
10
5
0
-5
(c)
Slip contour at 100 days
Slip contour at 50 days
Slip contour at 25 days
Cumulative slip (m)
0.2
0.4
0.6
0.8

Figure 10.

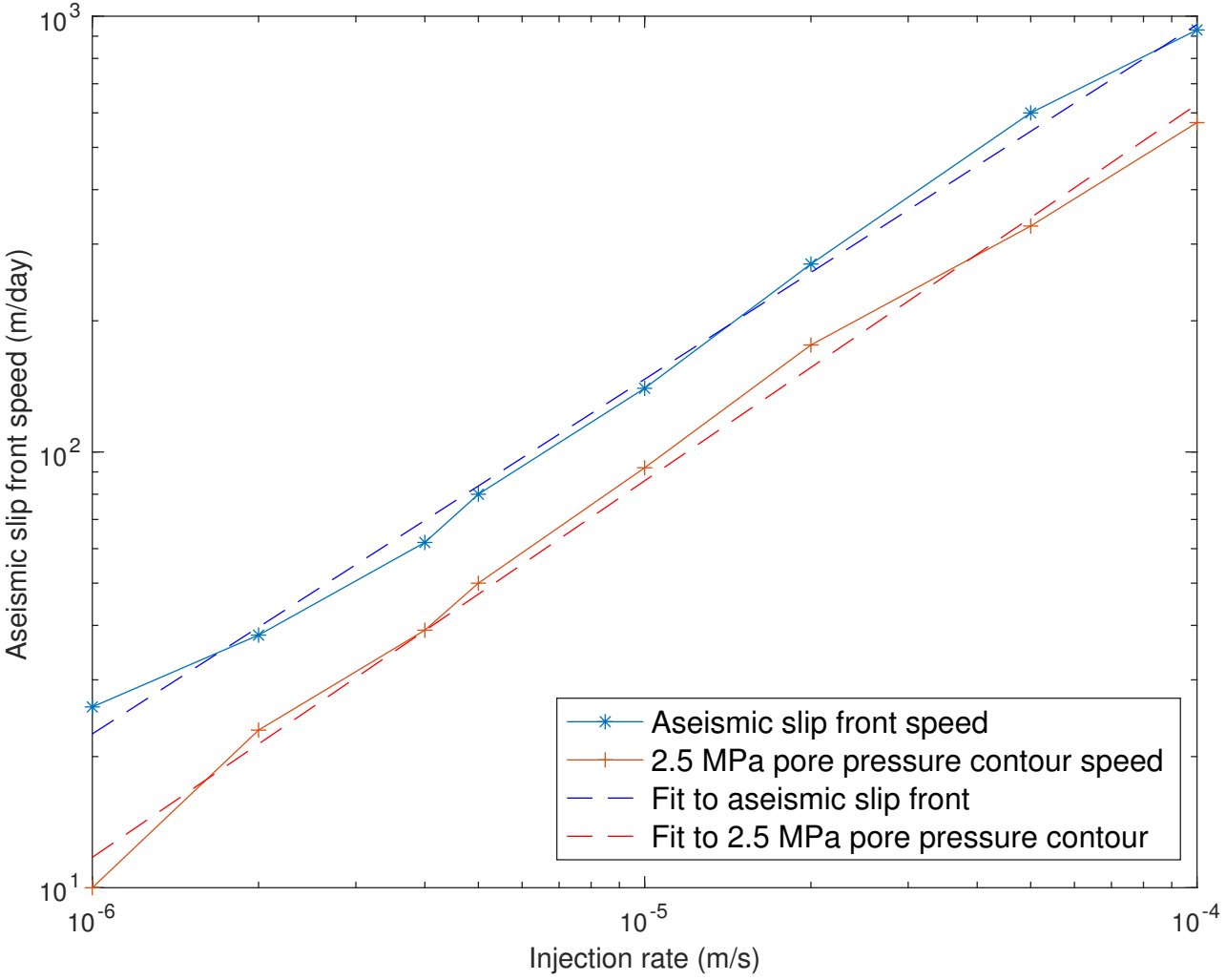
10^3
10^2
10^1
Aseismic slip front speed (m/day)
10^{-6}
10^{-5}
10^{-4}
Injection rate (m/s)
Aseismic slip front speed
2.5 MPa pore pressure contour speed
Fit to aseismic slip front
Fit to 2.5 MPa pore pressure contour

Figure 11.

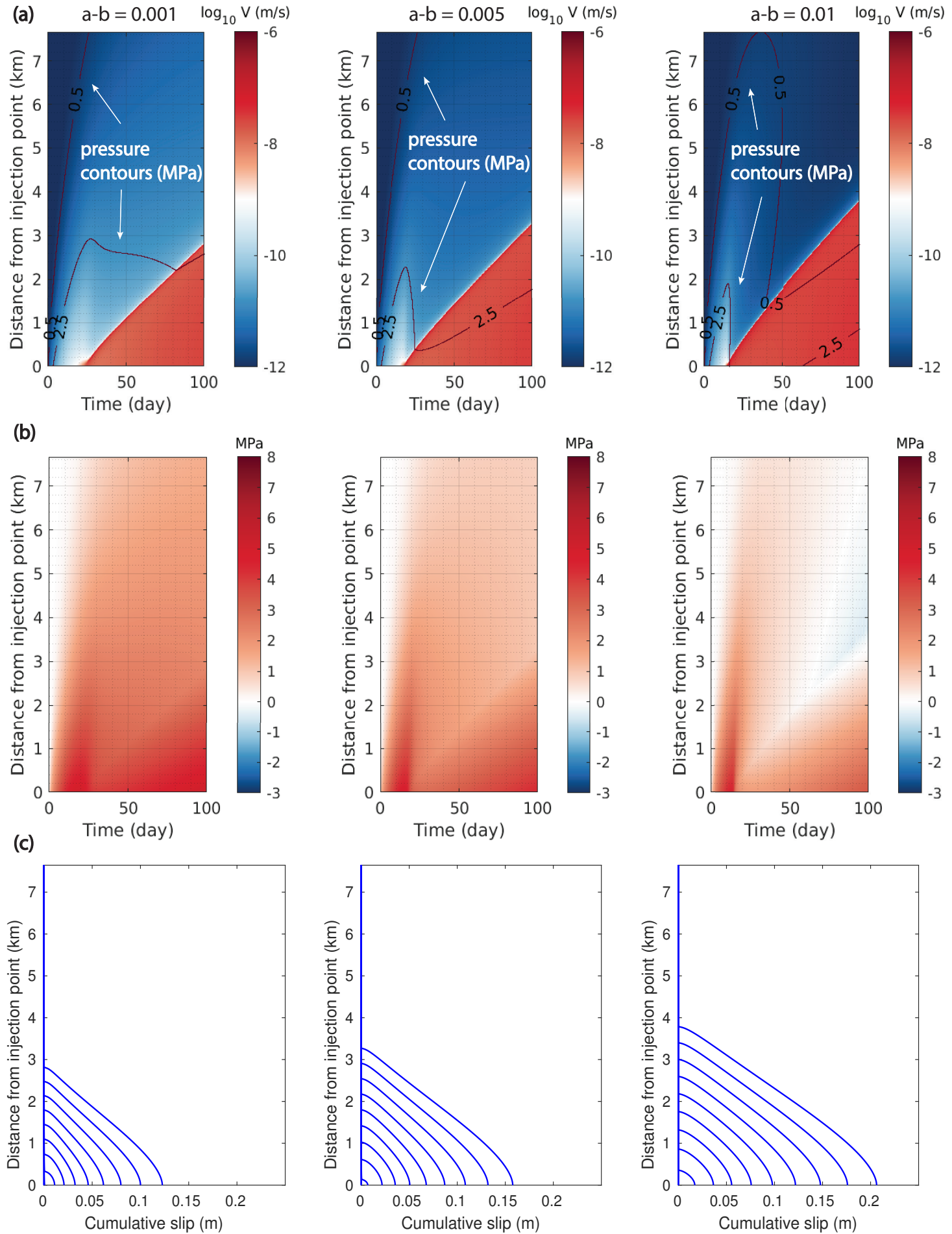
(a)
a-b = 0.001
a-b = 0.005
a-b = 0.01
log10 V (m/s)
pressure contours (MPa)
Distance from injection point (km)
Time (day)
(b)
MPa
(c)
Cumulative slip (m)

Figure 12.

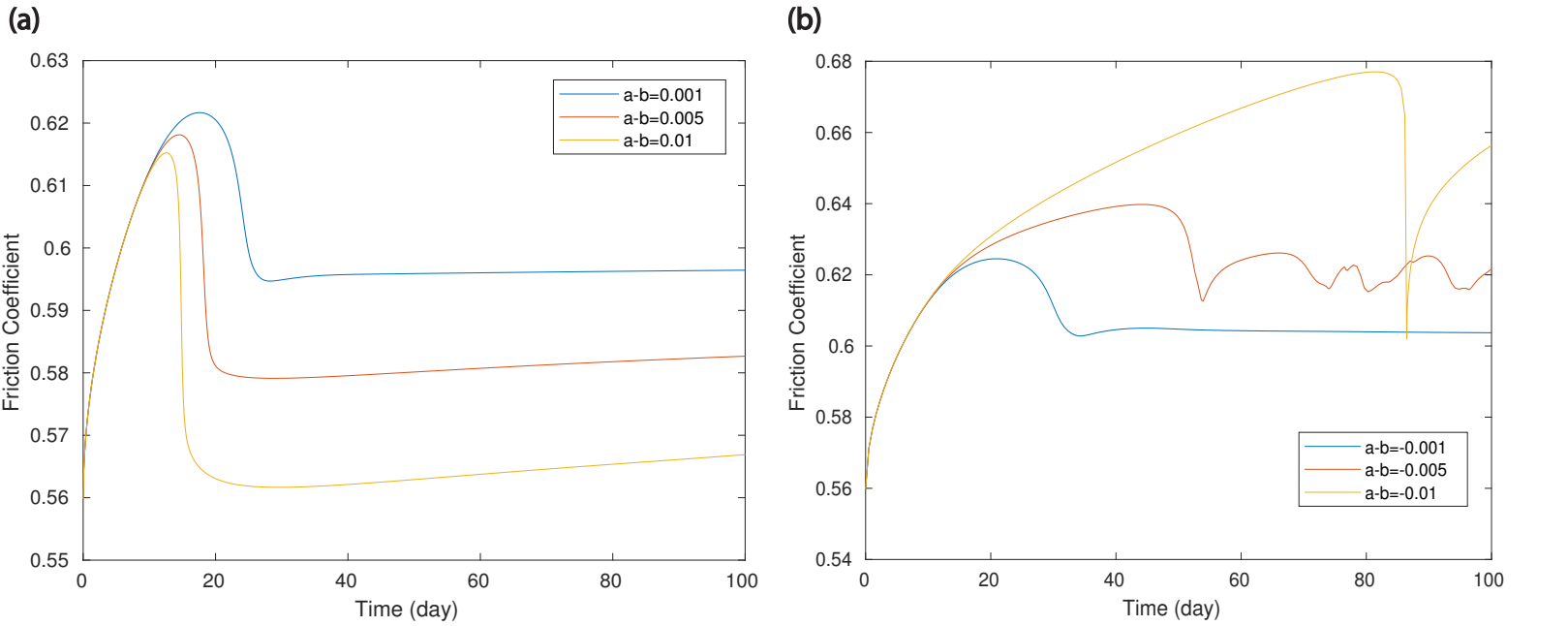
(a)
Friction Coefficient
Time (day)
a-b=0.001
a-b=0.005
a-b=0.01
0.63
0.62
0.61
0.6
0.59
0.58
0.57
0.56
0.55
0
20
40
60
80
100
(b)
Friction Coefficient
Time (day)
a-b=-0.001
a-b=-0.005
a-b=-0.01
0.68
0.66
0.64
0.62
0.6
0.58
0.56
0.54
0
20
40
60
80
100

Figure 13.

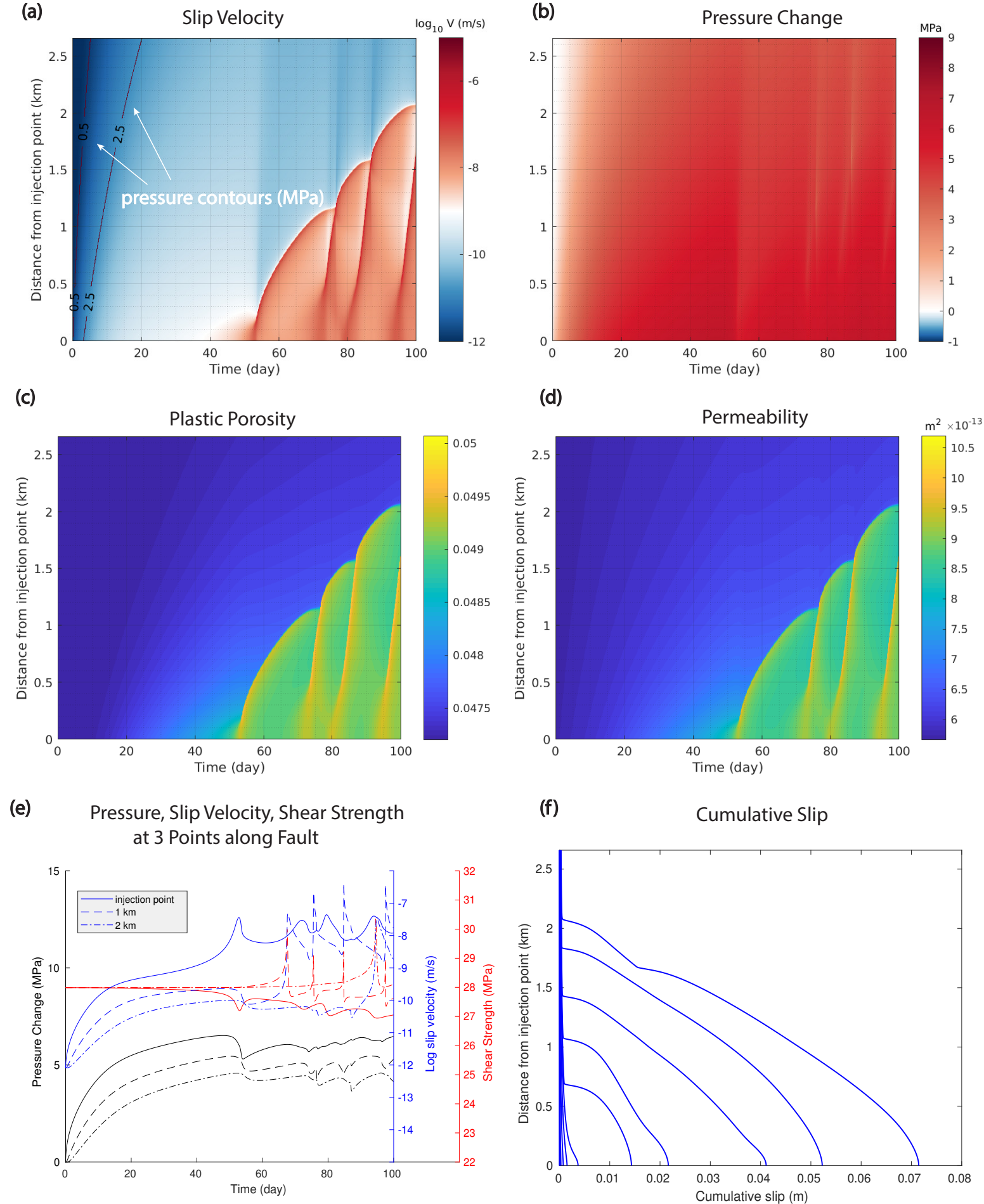
(a)
Slip Velocity
log10 V (m/s)
pressure contours (MPa)
0.5
2.5
Distance from injection point (km)
Time (day)
(b)
Pressure Change
MPa
Time (day)
(c)
Plastic Porosity
Distance from injection point (km)
Time (day)
(d)
Permeability
m2 ×10-13
Distance from injection point (km)
Time (day)
(e)
Pressure, Slip Velocity, Shear Strength
at 3 Points along Fault
injection point
1 km
2 km
Pressure Change (MPa)
Log slip velocity (m/s)
Shear Strength (MPa)
Time (day)
(f)
Cumulative Slip
Distance from injection point (km)
Cumulative slip (m)

Figure 14.

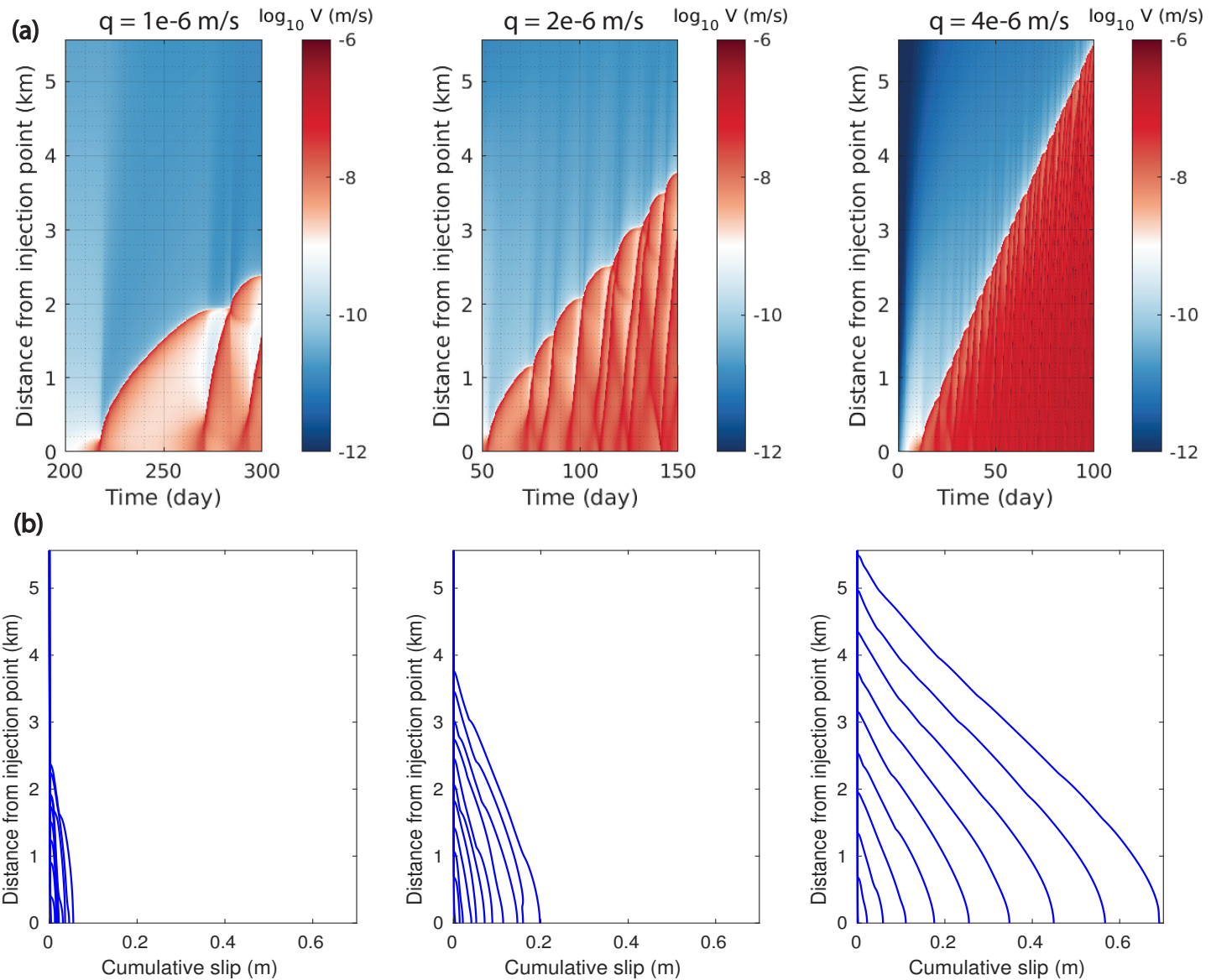
(a)
q = 1e-6 m/s
q = 2e-6 m/s
q = 4e-6 m/s
log10 V (m/s)
Distance from injection point (km)
Time (day)
(b)
Cumulative slip (m)